Dynamics and sound radiation of a dielectric elastomer membrane

Emil Garnell, Corinne Rouby, Olivier Doaré

Dynamics and sound radiation of a dielectric elastomer membrane

Emil Garnell[a], Corinne Rouby[a], Olivier Doaré[a]

[a]*IMSIA, ENSTA Paris, Institut Polytechnique de Paris, 828 boulevard des Maréchaux, 91120 Palaiseau.*

Abstract

This paper investigates sound radiation by an inflated dielectric elastomer membrane. The constitutive equations of the coupled electromechanical system are derived from general mechanical equilibrium equations, from Maxwell's equations, and from thermodynamic considerations. A finite deformation model featuring a hyperelastic constitutive law is written for the case of a thin membrane. The static finite deformation obtained when the membrane is inflated and when a voltage is applied is computed. The linear dynamics around this equilibrium are studied on the modal basis: the mode shapes and eigenfrequencies are computed, as well as the modal forces created by the voltage applied on the electrodes. The radiated acoustic pressure is estimated using a modified Rayleigh integral to take into account curvature effects. All numerical calculations are validated against measurements. The model is shown to be able to predict the linear vibrations, as well as the radiated pressure. The effect of the volume of the cavity on which the membrane is inflated is taken into account in the model. This model can therefore be used to optimize the design of dielectric loudspeakers, in terms of spectral balance for example.

Keywords:
Dielectric elastomer, Loudspeaker, Electro-mechanical coupling, Modal-analysis

1. Introduction

Dielectric elastomer membranes are made of a soft elastomer material sandwiched between two compliant electrodes. When a high voltage is applied to the electrodes, the attraction of the opposite charges causes the contraction of the elastomer in the thickness direction. As this material is almost incompressible this will result in an increase in the membrane area. This principle allows electromechanical conversion, that is at the core of many applications. Dielectric elastomers have raised a large interest since year 2000 when Pelrine et al. showed that strains greater than 100% caused by electric actuation could be achieved [1]. A wide range of applications has next been considered: micro-pumps [2], artificial muscles [3], tactile displays [4], energy harvesting [5], etc. Research works investigating their use as sound reproduction devices followed [6, 7, 8]. This article is focused on the latter application.

The most common configuration for the use of dielectric elastomer as loudspeakers builds on the change in area described above: if the thin membrane is inflated over a finite volume, a change in area induced by the imposed electric field will create a displacement normal to the membrane (see Fig. 2). This configuration has been suggested and studied by Heydt et al. [6], who presented the first acoustic radiation experimental results. A very simple model was presented by the same research group to predict qualitatively the radiated acoustic pressure [7]. The authors found that the primary resonance of the inflated membrane is strongly influenced by the volume on which the membrane is inflated. Moreover, the inflation pressure was shown to influence the directivity [9]. More detailed experimental studies of the dynamics of an inflated dielectric membrane were carried out by Fox and Goulbourne [8, 10]. They studied the low frequency range (below 200 Hz), and analysed the influence of the major design parameters on the first resonance frequencies. They showed that the dynamics of the structure do not comply with classical dynamics with Rayleigh real modes, *i.e.* different points of the membrane reach their maximum displacement at different times. Additionally, the casing volume was found to have a strong influence on the eigenmodes and eigenfrequencies of the

Email addresses: emil.garnell@ensta-paris.fr (Emil Garnell), corinne.rouby@ensta-paris.fr (Corinne Rouby), olivier.doare@ensta-paris.fr (Olivier Doaré)

membrane. In the same context, the experimental work of Hosoya et al. [11] allowed to characterise the directivity of a membrane inflated to a hemisphere. This system was found to be omnidirectionnal up to high frequencies (16 kHz).

The aforementioned researches were mainly focused on experiments. Let us now review the different modeling works found in the literature. A non-linear model for the static inflation has been derived by Fox and Goulbourne [10]. In the context of the transition between multiple static equilibrium positions of an inflated membrane, a time domain model was proposed by Mockensturm and Goulbourne [12]. The first complete theoretical study of the dynamics of an inflated membrane was carried out by Zhu et al. [13, 14]. The linear modes around a non-linear static equilibrium were computed, and the frequencies were compared to those found by Fox and Goulbourne [10]. However this model does not include the effect of the casing volume: the inflation pressure was assumed to be fixed. Consequently, these results cannot be directly compared to Fox and Goulbourne's experimental observations.

More recently Li et al. [15] studied both experimentally and numerically the mode shapes and resonance frequencies of a dielectric elastomer resonator made of a stretched membrane with added passive patches. However their configuration is not designed for sound reproduction (no inflation pressure), as they were not interested in sound radiation.

Other authors investigated the effect of viscosity on the dynamics of dielectric elastomer membranes (eg. [16, 17, 18, 19]). Those studies are carried out in the time domain, to describe accurately the displacement caused by a given applied voltage. Consequently, these approaches are limited to the low frequency behavior and can be time consuming if transfer functions are to be computed.

In the present article, we consider a dielectric elastomer loudspeaker as described by other authors: a dielectric elastomer membrane is inflated over a closed cavity so that the application of a variable voltage to the electrodes radiates acoustic pressure. Schematics of the studied system are given in section 3 in Fig. 2. Our objective is to develop a model taking into account all key phenomena and capable of predicting the radiated pressure.

The problem is highly non-linear [13], which is undesirable for a faithful sound reproduction. Nevertheless, if the excitation signal is cleverly chosen (see [7, 20]), the dynamics will be dominated by linear terms. We therefore choose to linearize the dynamics of the system. Even in this simplified framework, important properties can be studied: spectral balance, directivity, efficiency.... Moreover, in order to run optimization routines, the model should allow fast computations of transfer functions between the excitation voltage and the radiated acoustic pressure. Thus, a model in the frequency domain is here derived.

This article is organised as follows. In section 2 the constitutive equations of a dielectric elastomer membrane are derived. Readers not interested in these details should jump to section 3 where the problem's equations are developed. The numerical method used to solve these equations is presented in section 4. The different steps are the computation of the linear modes around a non-linear static equilibrium, the derivation of the modal forces created by the electromechanical loading, and the computation of the transfer functions between the excitation voltage and the dynamics or the acoustics. The results are compared to experiments in section 5, and the influence of the major parameters is discussed in the last section 6.

2. Constitutive equations of the dielectric elastomer membrane

2.1. General 3D case

The first step is to derive the constitutive equations of a dielectric elastomer. This is carried out in a general 3D framework, and will be simplified to membrane kinematics afterwards. We summarize here the derivation of the constitutive relations using the Coleman-Noll method [21], which is a general framework for writing multi-physics constitutive equations [22, 23, 24], starting from balance equations and thermodynamic principles.

We consider a dielectric body partially covered by electrodes on its surface. In the absence of any electric charge or mechanical load, the body occupies a reference configuration, where each material particle is identified by its position $\mathbf{X}$. Under electrical and mechanical loading, the body is transformed to a deformed configuration: the material point initially in $\mathbf{X}$ moves to the position $\mathbf{X}$. The deformation gradient tensor is defined by $\mathbf{F} = \partial\mathbf{X}/\partial\mathbf{X}$. In the deformed configuration, body forces $\mathbf{F}$ and surface forces $\mathbf{t_s}$ are applied to the body, as well as electric surface charges σ_s. It is assumed that there is no electric body charge. The problem is sketched in Fig. 1. The mass density is denoted by ρ, the Cauchy stress tensor by $\boldsymbol{\sigma}$, and the electric displacement by $\mathbf{d} = \epsilon_0\mathbf{e} + \mathbf{p}$, where ϵ_0 is the vacuum permittivity, $\mathbf{e}$ the

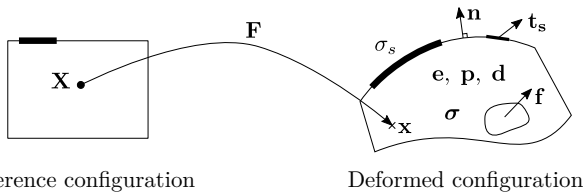

Figure 1: Description of a material sample and definition of external loads

electric field and $\mathbf{p}$ the electric polarization density, all in the deformed configuration. The Lagrangian time derivative $\mathrm{d}/\mathrm{d}t$ is written $\dot{(\cdot)}$, and the notation $\boldsymbol{\nabla} = \partial/\partial\mathbf{X}$ is introduced.

If the resistivity of the electrodes is low enough, the time scale for electrodynamic effects is much shorter than that for mechanics. It is therefore assumed that Maxwell's equations for electrostatics hold. The local electrostatic equations (Gauss and Faraday), linear momentum balance and mass conservation are thus:

$$\boldsymbol{\nabla}\cdot\mathbf{d} = 0\,, \qquad \boldsymbol{\nabla}\times\mathbf{e} = \mathbf{0}\,, \qquad \rho\ddot{\mathbf{X}} = \boldsymbol{\nabla}\cdot\boldsymbol{\sigma} + \rho\mathbf{F}\,, \qquad \dot{\rho} + \rho\boldsymbol{\nabla}\cdot\dot{\mathbf{x}} = 0\,. \tag{1}$$

The related jump conditions on the boundaries are:

$$\mathbf{n}\cdot[\![\mathbf{d}]\!] = \sigma_s\,, \qquad \mathbf{n}\times[\![\mathbf{e}]\!] = \mathbf{0}\,, \qquad \mathbf{n}\cdot[\![\boldsymbol{\sigma}]\!] + \mathbf{t_s} = \mathbf{0}\,, \tag{2}$$

where $\mathbf{n}$ denotes the normal to the surface and $[\![a]\!] = a(x^+) - a(x^-)$, x^+ and x^- being points just outside and inside of the surface respectively.

In the following, we search for a constitutive relation compatible with the local balance equations (1) and (2). Thermodynamic principles will restrict the expression of the constitutive relation: the global energy balance and entropy imbalance need to be satisfied. They read, for any arbitrary region $\Omega \subset \mathbb{R}^3$ of boundary $\partial\Omega$:

$$\frac{\mathrm{d}}{\mathrm{d}t}\left(\int_\Omega \rho\varepsilon \mathrm{d}\Omega\right) = \int_\Omega \mathbf{F}\cdot\dot{\mathbf{X}}\rho\mathrm{d}\Omega - \int_{\partial\Omega}(\boldsymbol{\sigma}\cdot\mathbf{n})\cdot\dot{\mathbf{X}}\mathrm{d}A + \int_\Omega \rho\vartheta\mathrm{d}\Omega + \int_{\partial\Omega} -\mathbf{q}\cdot\mathbf{n}\mathrm{d}A - \int_{\partial\Omega}\mathbf{e}\times(\dot{\mathbf{X}}\times\mathbf{d})\cdot\mathbf{n}\mathrm{d}A\,, \tag{3}$$

$$\frac{\mathrm{d}}{\mathrm{d}t}\left(\int_\Omega \rho\eta \mathrm{d}\Omega\right) \geq \int_\Omega \rho\vartheta\theta_T^{-1}\mathrm{d}\Omega + \int_{\partial\Omega} -\mathbf{q}\cdot\mathbf{n}\theta_T^{-1}\mathrm{d}A\,, \tag{4}$$

where ε is the total energy per unit mass, $\mathbf{q}$ the heat flux, ϑ the volumic heat source, η the entropy, and θ_T the temperature. The two first terms on the right hand side of Eq. (3) are the mechanical power, the two next ones the thermal power, and the last one the electrostatic power.

Using Eq. (1) in Eqs. (3) and (4), applying the divergence theorem and using vector identities yields the local energy balance and entropy imbalance:

$$\rho\dot{\varepsilon} = \rho(\dot{\mathbf{X}}\cdot\ddot{\mathbf{X}} + \vartheta) + [\boldsymbol{\sigma} - \mathbf{d}\otimes\mathbf{e} + (\mathbf{e}\cdot\mathbf{d})\mathbf{I}]\colon\dot{\mathbf{F}} + \mathbf{e}\cdot\dot{\mathbf{d}} - \boldsymbol{\nabla}\cdot\mathbf{q}\,, \tag{5}$$

$$\rho\dot{\eta} \geq \rho\vartheta\theta_T^{-1} - \boldsymbol{\nabla}\cdot\left(\mathbf{q}{\theta_T}^{-1}\right)\,. \tag{6}$$

Replacing the heat source ϑ in Eq. (6) using Eq. (5) yields:

$$-\rho\dot{\varepsilon} + \rho(\theta_T\dot{\eta} + \dot{\mathbf{X}}\cdot\ddot{\mathbf{X}}) + [\boldsymbol{\sigma} - \mathbf{d}\otimes\mathbf{e} + (\mathbf{e}\cdot\mathbf{d})\mathbf{I}]\colon\dot{\mathbf{F}} + \mathbf{e}\cdot(\epsilon_0\dot{\mathbf{e}} + \dot{\mathbf{p}}) - {\theta_T}^{-1}\mathbf{q}\cdot(\boldsymbol{\nabla}\theta_T) \geq 0\,. \tag{7}$$

This equation shows that variations of the internal energy ε are related to variations of $\dot{\mathbf{X}}$, $\mathbf{F}$, $\mathbf{e}$, $\mathbf{p}$ and η. Therefore, ε must be a function of those five variables only, or of five independent combinations of them. Computing the derivatives of ε and inserting into the entropy imbalance Eq. (7) yields:

$$\rho\left[\left(\theta_T - \frac{\partial\varepsilon}{\partial\eta}\right)\dot{\eta} + \ddot{\mathbf{X}}\cdot\left(\dot{\mathbf{X}} - \frac{\partial\varepsilon}{\partial\dot{\mathbf{X}}}\right)\right] + \left[-\rho\left(\frac{\partial\varepsilon}{\partial\mathbf{F}}\cdot\mathbf{F}^T\right)^T + \boldsymbol{\sigma} - \mathbf{d}\otimes\mathbf{e} + (\mathbf{e}\cdot\mathbf{d})\mathbf{I}\right]\colon\dot{\mathbf{F}}$$
$$+\left(\epsilon_0\mathbf{e} - \rho\frac{\partial\varepsilon}{\partial\mathbf{e}}\right)\cdot\dot{\mathbf{e}} + \left(\mathbf{e} - \rho\frac{\partial\varepsilon}{\partial\mathbf{p}}\right)\cdot\dot{\mathbf{p}} - {\theta_T}^{-1}\mathbf{q}\cdot(\boldsymbol{\nabla}\theta_T) \geq 0\,. \tag{8}$$

As $\dot{\mathbf{X}}$, $\mathbf{F}$, $\mathbf{e}$, $\mathbf{p}$ and η are independent variables that can take arbitrary values, the internal energy ε must satisfy the following equations:

$$\frac{\partial \varepsilon}{\partial \eta} = \theta_T \ , \qquad \frac{\partial \varepsilon}{\partial \dot{\mathbf{X}}} = \dot{\mathbf{X}} \ , \qquad \rho\left(\frac{\partial \varepsilon}{\partial \mathbf{F}} \cdot \mathbf{F}^T\right)^T = \boldsymbol{\sigma} - \mathbf{d} \otimes \mathbf{e} + (\mathbf{e} \cdot \mathbf{d})\mathbf{I} \ , \qquad \rho\frac{\partial \varepsilon}{\partial \mathbf{e}} = \epsilon_0 \mathbf{e} \ , \qquad \rho\frac{\partial \varepsilon}{\partial \mathbf{p}} = \mathbf{e} \ , \tag{9}$$

and the heat flux $\mathbf{q}$ is restricted by the condition ${\theta_T}^{-1}\mathbf{q} \cdot (\boldsymbol{\nabla}\theta_T) \leq 0$. For a given expression of ε in terms of $\dot{\mathbf{X}}$, $\mathbf{F}$, $\mathbf{e}$, $\mathbf{p}$ and η, Eqs. (9) specify the constitutive relations of the coupled system. These equations can be simplified, by defining the free energy ψ:

$$\psi = \varepsilon - \frac{1}{2}\dot{\mathbf{X}} \cdot \dot{\mathbf{X}} - \eta\theta_T - \frac{\epsilon_0}{2\rho}\mathbf{e} \cdot \mathbf{e} - \frac{1}{\rho}\mathbf{e} \cdot \mathbf{p} \ . \tag{10}$$

Computing the derivatives of ψ in terms of the derivatives of ε, and using Eqs. (9) allows to show that ψ is a function of $\mathbf{F}$, $\mathbf{e}$, and θ_T only. Finally the expression of ε in terms of ψ can be substituted into Eq. (7), yielding:

$$\rho\left(-\left(\frac{\partial \psi}{\partial \mathbf{e}} + \frac{\mathbf{p}}{\rho}\right) \cdot \dot{\mathbf{e}} - \left(\frac{\partial \psi}{\partial \theta_T} + \eta\right)\dot{\theta_T}\right) + \left[-\rho\left(\frac{\partial \psi}{\partial \mathbf{F}} \cdot \mathbf{F}^T\right)^T + \boldsymbol{\sigma} - \mathbf{d} \otimes \mathbf{e} + \frac{\epsilon_0}{2}(\mathbf{e} \cdot \mathbf{e})\mathbf{I}\right] : \dot{\mathbf{F}} - {\theta_T}^{-1}\mathbf{q} \cdot (\boldsymbol{\nabla}\theta_T) \geq 0 \ . \tag{11}$$

And again for the energy imbalance Eq. (11) to hold for any arbitrary evolution, the following equations need to be satisfied:

$$\frac{\partial \psi}{\partial \mathbf{e}} = -\frac{\mathbf{p}}{\rho} \ , \qquad \frac{\partial \psi}{\partial \theta_T} = -\eta \ , \qquad \boldsymbol{\sigma} = \rho\left(\frac{\partial \psi}{\partial \mathbf{F}} . \mathbf{F}^T\right)^T + \mathbf{d} \otimes \mathbf{e} - \frac{\epsilon_0}{2}(\mathbf{e} \cdot \mathbf{e})\mathbf{I} \ . \tag{12}$$

We now assume that the transformation is isotherm, which removes the dependence on θ_T of the free energy. The principle of material frame invariance [22] implies that the free energy should depend only on the Cauchy-Green tensor $\mathbf{C} = \mathbf{F}^T \cdot \mathbf{F}$ and on the electric field in reference configuration $\mathbf{e} = \mathbf{F}^T \cdot \mathbf{e}$, that is to say $\psi(\mathbf{F}, \mathbf{e}) = \phi(\mathbf{C}, \mathbf{e})$. Equating variations of ψ and ϕ yields :

$$\boldsymbol{\sigma} = 2\rho\mathbf{F} \cdot \frac{\partial \phi}{\partial \mathbf{C}} \cdot \mathbf{F}^T + \epsilon_0 \mathbf{e} \otimes \mathbf{e} - \frac{\epsilon_0}{2}(\mathbf{e} \cdot \mathbf{e})\mathbf{I} \ , \qquad \mathbf{p} = -\rho\mathbf{F} \cdot \frac{\partial \phi}{\partial \mathbf{e}} \ . \tag{13}$$

Equations Eqs. (13) are the two constitutive equations giving the material behavior, which is fully described by the specification of the free energy function ϕ. The first resembles the classical mechanical equation relating the Cauchy stress tensor to the free energy, but with added terms that depend on electrostatics. Following the method of Edminston and Steigmann [23], a realistic free energy function is now searched for. In this step, we aim at reproducing behaviors that have been observed experimentally. Typical dielectric elastomers have been shown to be linear for the electrostatics (the material polarization $\mathbf{p}$ is proportional to the electric field $\mathbf{e}$, meaning that the permittivity ϵ does not depend on the deformation). This class of materials is called *ideal dielectric elastomers* by Suo [25]. Also, when no electric field is applied, the material should behave as a standard hyperelastic material. Therefore, a free energy function that satisfies the two following conditions is searched for:

$$\mathbf{p} = \epsilon_0 \chi_e \mathbf{e} \ , \tag{14}$$

$$\boldsymbol{\sigma} = \rho\left(2\mathbf{F} \cdot \frac{\partial \phi_0}{\partial \mathbf{C}} \cdot \mathbf{F}^T\right)^T \quad \text{when } \mathbf{e} = 0 \ , \tag{15}$$

where ϕ_0 is a purely mechanical free energy. We suggest the following form of the free energy, which fulfills the two conditions:

$$\phi(\mathbf{C}, \mathbf{e}, \Pi) = \phi_0(\mathbf{C}) - \frac{\epsilon_0 \chi_e J}{2\rho_0}\mathbf{e} \cdot \mathbf{C}^{-1} \cdot \mathbf{e} \ . \tag{16}$$

For this specific form of the free energy, Eq. (13) implies that the total stress is the sum of a purely mechanical stress $\boldsymbol{\sigma}_0$ and a Maxwell stress:

$$\boldsymbol{\sigma} = \boldsymbol{\sigma}_0 + \boldsymbol{\sigma}_{\text{Maxwell}} \ , \qquad \text{with } \boldsymbol{\sigma}_0 = 2\rho_0\mathbf{F} \cdot \frac{\partial \phi_0}{\partial \mathbf{C}} \cdot \mathbf{F}^T \ , \qquad \text{and } \boldsymbol{\sigma}_{\text{Maxwell}} = \epsilon\left(\mathbf{e} \otimes \mathbf{e} - \frac{1}{2}\mathbf{e} \cdot \mathbf{e}\mathbf{I}\right) \ , \tag{17}$$

where $\epsilon = \epsilon_0(1 + \chi_e)$. Equations (17) are a well known set of equations that are used by most people working with dielectric elastomers. However, they have here been thoroughly derived starting from general equilibrium equations, making clear the assumptions that have been made to obtain these equations. The distinction between the mechanical and the Maxwell stress appears to have no importance, as all equilibrium equations depend on the total stress $\boldsymbol{\sigma}$.

2.2. Reduction of the constitutive equations to the case of a membrane

In the previous section the constitutive laws of the dielectric elastomer have been established, in the general 3D case. In the case of a membrane they can be significantly simplified.

Concerning the electrostatics, the classical approximation for a thin dielectric between electrodes is made: the electric field is assumed to be normal to the membrane, and null outside of the dielectric. Fringe effects are neglected. This leads to:

$$\mathbf{e} = e\mathbf{n} \,, \qquad \text{with } e = \frac{U}{h} \,, \tag{18}$$

where $\mathbf{n}$ is the normal to the membrane, h the thickness of the membrane, and U the electric potential difference between the electrodes. The electric field e does not vary in the thickness direction.

A specific form of the mechanical free energy now needs to be chosen. In the following the elastomer is assumed to behave according to the Gent material law [26] (this assumption will be validated in the experimental section 5.2.2), and a Lagrange multiplier Π is used to impose the incompressibility constraint $J = 1$:

$$\phi_0 = -\frac{\mu J_m}{2} \ln\left(1 - \frac{I_1 - 3}{J_m}\right) + \frac{\Pi}{\rho_0}(J - 1) \,, \tag{19}$$

where $I_1 = \operatorname{tr}\mathbf{C}$ is the first invariant of the Cauchy-Green tensor, μ is the shear modulus, and J_m is a parameter describing the stiffening of the material at large strains. In the principal basis, the deformation gradient and the right Cauchy-Green deformation tensor read:

$$\mathbf{F} = \lambda_1 \mathbf{u_1} \otimes \mathbf{u_1} + \lambda_2 \mathbf{u_2} \otimes \mathbf{u_2} + \lambda_n \mathbf{n} \otimes \mathbf{n} \,, \tag{20}$$

$$\mathbf{C} = \mathbf{F}^T\mathbf{F} = \lambda_1^2 \mathbf{u_1} \otimes \mathbf{u_1} + \lambda_2^2 \mathbf{u_2} \otimes \mathbf{u_2} + \lambda_n^2 \mathbf{n} \otimes \mathbf{n} \,, \tag{21}$$

where λ_1 and λ_2 are the two main planar stretches and λ_n the normal stretch. Putting Eqs. (18)-(21) into Eq. (17) provides the expression of $\boldsymbol{\sigma}$ in the principal basis ($\boldsymbol{\sigma} = \sigma_1 \mathbf{u_1} \otimes \mathbf{u_1} + \sigma_2 \mathbf{u_2} \otimes \mathbf{u_2} + \sigma_n \mathbf{n} \otimes \mathbf{n}$):

$$\sigma_1 = \frac{\mu J_m}{J_m - I_1 + 3}\lambda_1^2 - \frac{\epsilon e^2}{2} + \Pi \,, \qquad \sigma_2 = \frac{\mu J_m}{J_m - I_1 + 3}\lambda_2^2 - \frac{\epsilon e^2}{2} + \Pi \,, \qquad \sigma_n = \frac{\mu J_m}{J_m - I_1 + 3}\lambda_n^2 + \frac{\epsilon e^2}{2} + \Pi \,. \tag{22}$$

The mechanical equilibrium equations are exactly the same as classical purely mechanical equations. The coupling with electrostatics appears only in the constitutive relation defining the stress. Therefore, classical membrane equations can be used, in which plane stress is assumed: $\boldsymbol{\sigma} \cdot \mathbf{n} = \sigma_n = 0$ [27]. This provides the expression for the Lagrange multiplier Π. Finally, the constitutive equations for the principal planar strains of a dielectric elastomer membrane are obtained:

$$\sigma_1 = \frac{\mu J_m}{J_m - I_1 + 3}\left(\lambda_1^2 - \lambda_n^2\right) - \epsilon e^2 \,, \tag{23}$$

$$\sigma_2 = \frac{\mu J_m}{J_m - I_1 + 3}\left(\lambda_2^2 - \lambda_n^2\right) - \epsilon e^2 \,, \tag{24}$$

where $e = U/h$, and $I_1 = \lambda_1^2 + \lambda_2^2 + \lambda_n^2$. The stretches are linked by the incompressibility relation $\lambda_1\lambda_2\lambda_n = 1$. Here one may notice that due to incompressibility the electromechanical coupling results in an increased stress in the planar directions that is twice the commonly called Maxwell pressure $P_{\text{maxwell}} = \epsilon e^2/2$. This is due to the coupling between the normal and planar deformations of the membrane.

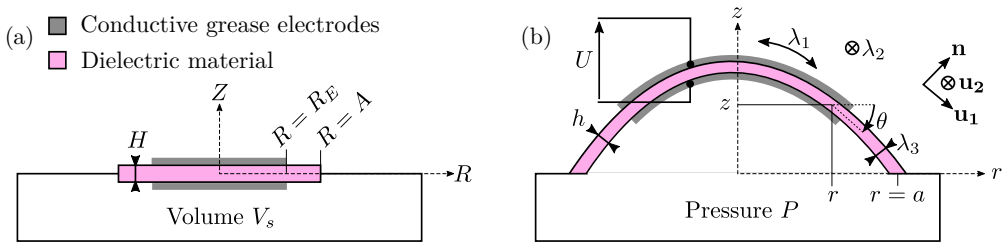

Figure 2: Schematics of the studied system. (a) Reference configuration, where the membrane is flat. In the example shown, $\Gamma(R) = 1$ for $R < R_E$ and $\Gamma(R) = 0$ for $R > R_E$. (b) Deformed configuration, where the membrane is stretched and inflated.

3. Formulation of the coupled electromechanical problem

3.1. Description of the studied system

We now return to the problem of the dynamics of a dielectric elastomer membrane in an inflated configuration, as sketched in Fig. 2. Only axisymmetric deformations are studied in the present work. The thickness of the membrane as well as the electrodes can be of any axisymetrical shape. The function $\Gamma(R)$ describes the electrode location: it equals unity when electrodes are present at radius R in the reference configuration (Fig. 2(a)), and zero otherwise. The membrane is pre-stretched from the radius A to a radius a and inflated with the pressure P. A voltage U is then applied between the electrodes. The material points of the membrane identified by the radius R in the reference configuration move to the radius $r(R,t)$ and the altitude $z(R,t)$ in the deformed configuration at time t (Fig. 2(b)). The corresponding radial and orthoradial stretches are denoted by λ_1 and λ_2 respectively. The principal stretches as well as the angle of incline θ, defined in Fig. 2(b), can be expressed in terms of the variables r and z:

$$\lambda_1 = \sqrt{\left(\frac{\partial r}{\partial R}\right)^2 + \left(\frac{\partial z}{\partial R}\right)^2}\,, \qquad \lambda_2 = \frac{r}{R}\,, \qquad \lambda_n = \frac{1}{\lambda_1\lambda_2} = \frac{h}{H}\,, \qquad \cos\theta = \frac{1}{\lambda_1}\frac{\partial r}{\partial R}\,, \qquad \sin\theta = \frac{1}{\lambda_1}\frac{\partial z}{\partial R}\,, \tag{25}$$

where H and h are the inhomogeneous thickness of the membrane in reference and deformed configuration respectively.

3.2. Equilibrium equations of the membrane

The dynamic equilibrium equations are derived from the classical membrane equations, commonly written along the normal and the tangential directions [28]. Given the axisymmetry of the problem, they are here projected along the radial and the vertical directions:

$$\rho(1 + \Gamma\rho_{\text{ratio}})\frac{rh}{\cos\theta}\frac{\partial^2 r}{\partial t^2} = -\frac{\sigma_2 h}{\cos\theta} - Pr\frac{\sin\theta}{\cos\theta} + \frac{\partial}{\partial r}(\sigma_1 rh\cos\theta)\,, \tag{26}$$

$$\rho(1 + \Gamma\rho_{\text{ratio}})\frac{rh}{\cos\theta}\frac{\partial^2 z}{\partial t^2} = Pr + \frac{\partial}{\partial r}\left(\sigma_1 rh\sin\theta\right)\,, \tag{27}$$

where ρ_{ratio} is the ratio of the electrode over the membrane mass per unit area. The dependence in radius R and time t of r, z, θ, h has been omitted for clarity. These equations are the same as those derived by Zhu et al. [14], and are similar to those used by Mockensturm and Goulbourne [12], except that they neglect tangential inertia. If all inertia is neglected Eqs. (26) and (27) are equivalent to the well-known hyperelastic membrane equations derived by Atkins [27]. Note that the electrostatic coupling appears only in behavior equations, and not in equilibrium equations.

All the equations of the problem are now transformed into a non-dimensional form, by introducing non-dimensional variables, denoted with an over-bar ($\bar{\ }$):

$$R = A\bar{R}\,, \quad a = A\bar{a}\,, \quad r = A\bar{r}\,, \quad z = A\bar{z}\,, \quad H = H_0\bar{H}\,, \quad \sigma_1 = \mu\lambda_1\bar{s}_1\,, \quad \sigma_2 = \mu\lambda_2\bar{s}_2\,, \quad t = \sqrt{\frac{\rho}{\mu}}A\bar{t}\,, \tag{28}$$

where $\bar{s}_1$ and $\bar{s}_2$ are the nominal non-dimensional stresses, and $H_0 = H(0)$ is the thickness at the center. Using the geometrical relations Eqs. (25) and the definition of the non-dimensional parameters Eqs. (28) we obtain from Eqs. (23)-(27) the non dimensional equilibrium equations and constitutive relations:

$$\left(\frac{\bar{H}\bar{R}\bar{s}_1\bar{r}'}{\lambda_1}\right)' - \beta\bar{r}\bar{z}' - \bar{s}_2\bar{H} = \bar{H}\bar{R}\left(1 + \frac{\Gamma}{\bar{H}}\rho_{\text{ratio}}\right)\ddot{\bar{r}}\,, \tag{29}$$

$$\left(\frac{\bar{H}\bar{R}\bar{s}_1\bar{z}'}{\lambda_1}\right)' + \beta\bar{r}\bar{r}' = \bar{H}\bar{R}\left(1 + \frac{\Gamma}{\bar{H}}\rho_{\text{ratio}}\right)\ddot{\bar{z}}\,, \tag{30}$$

$$\bar{s}_1 = \frac{J_m}{J_m - I_1 + 3}\left(\lambda_1 - {\lambda_1}^{-3}{\lambda_2}^{-2}\right) - \alpha\frac{\Gamma}{\bar{H}^2}\lambda_1\lambda_2^2\,, \tag{31}$$

$$\bar{s}_2 = \frac{J_m}{J_m - I_1 + 3}\left(\lambda_2 - {\lambda_1}^{-2}{\lambda_2}^{-3}\right) - \alpha\frac{\Gamma}{\bar{H}^2}\lambda_1^2\lambda_2\,. \tag{32}$$

where $\beta = AP/\mu H_0$, and $\alpha = \epsilon U^2/\mu H_0^2$. The prime ($'$) stands for the space derivative $\partial/\partial\bar{R}$, and the dot ($\dot{}$) is the time derivative $\partial/\partial\bar{t}$. The electric field is non-zero only where the electrodes are located, as indicated by the factor Γ in Eqs. (31) and (32).

The last equations needed to close the problem are the boundary conditions. At the center the radial displacement is zero and the membrane slope is zero. The membrane is clamped at the outer edge at $R = A$. This reads:

$$\bar{r}(\bar{R} = 0) = 0\,, \qquad \bar{r}(\bar{R} = 1) = \bar{a}\,, \qquad \bar{z}'(\bar{R} = 0) = 0\,, \qquad \bar{z}(\bar{R} = 1) = 0\,. \tag{33}$$

The first stage of the considered problem consists in pre-stretching and inflating the membrane with the pressure P_{pres} (β_{pres} in non-dimensional form). During this step the amount or air in the cavity varies. In the second stage, the cavity is closed, and the volume under the membrane is then called $\bar{V}_{\text{ini}}$. The pressure inside the cavity changes with the membrane deformation, which adds a stiffness term to equilibrium equations. The transformation is assumed to be quick compared to heat exchange times, therefore the gas evolution inside the volume can be considered adiabatic. The ideal gas law implies that PV^γ is constant, where $\gamma = 1.4$ is the heat capacity ratio, and V the total volume of the cavity (including the volume under the membrane). This equation in non-dimensional form reads:

$$(\beta_{\text{atm}} + \beta)\left(\bar{V}_s + 2\pi\int \bar{r}\bar{z}\bar{r}'\mathrm{d}\bar{R}\right)^\gamma = \left(\beta_{\text{atm}} + \beta_{\text{pres}}\right)\left(\bar{V}_s + \bar{V}_{\text{ini}}\right)^\gamma\,, \tag{34}$$

where $\beta_{\text{atm}} = AP_{\text{atm}}/\mu H_0$, P_{atm} is the atmospheric pressure, $\bar{V}_s = V_s/A^3$, and V_s is the volume of the cavity when the membrane is not inflated. As a consequence, β is in the second stage a variable and not a fixed parameter, and one more equilibrium equation has to be solved (Eq. (34)).

3.3. Dynamic excitation by the electrodes

The Maxwell stress, which is responsible for the electromechanical activation, is proportional to the squared voltage (see Eqs. (17) and (18)). This will be the major source of non-linearities. However, shaping the input signal can help reducing distortion, as shown by Heydt et al. [7], and Kaal and Herold [20]. The following voltage is therefore applied to the electrode connections:

$$U_{\text{app}}(t) = \sqrt{{U_c}^2 + W_s(t)}\,, \qquad \text{with } {U_c}^2 > |W_s|\,, \tag{35}$$

where U_c is a DC voltage, and $W_s(t)$ an alternating component (in V^2) which corresponds to the audio signal that is played on the loudspeakers.

Moreover, the conductive grease used for the electrodes has a finite resistivity. As a consequence, at higher frequencies the effective voltage on the electrodes will no longer be uniform, and the average on the electrodes surface will be smaller than the voltage applied to their connections. The most simple way to account for this phenomenon is to build a lumped model of the membrane and its electrodes: its forms an RC circuit (see Fig. 3). The circuit is a

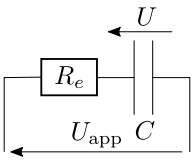

Figure 3: Simple electrical model of the dielectric elastomer membrane. R_e stands for the resistance of the electrodes, C is the capacity of the membrane plus electrodes capacitor, U_{app} the voltage applied to the electrodes connections, and U the effective voltage on the electrodes.

low-pass filter, whose transfer function in the frequency domain reads as:

$$\frac{\hat{U}}{\hat{U}_{\mathrm{app}}} = \frac{1}{1 + \mathrm{i}\frac{\omega}{\omega_{\mathrm{cut}}}} , \tag{36}$$

where $\omega_{\mathrm{cut}} = 1/R_eC$. In this section hats denote Fourier transforms ($\hat{U} = \mathcal{F}(U)$).

The first order effect of this filter on the voltage U_{app} applied to the electrodes is now estimated. For small amplitudes of W_s compared to ${U_c}^2$, the applied voltage can be linearized as:

$$U_{\mathrm{app}}(t) = \sqrt{{U_c}^2 + W_s(t)} \approx U_c + \frac{W_s(t)}{2U_c} . \tag{37}$$

Filtering U_{app} by the RC circuit Eq. (36) yields:

$$U(t) \approx U_c + \frac{1}{2U_c} W(t) , \qquad \text{with } W(t) = \mathcal{F}^{-1}\left(\frac{\hat{W}_s(\omega)}{1 + \mathrm{i}\frac{\omega}{\omega_{\mathrm{cut}}}} \right) , \tag{38}$$

where $\mathcal{F}^{-1}$ is the inverse Fourier transform. Finally, by squaring and keeping the first order term:

$$U^2(t) \approx U_c^2 + W(t) . \tag{39}$$

At low frequencies, $1 + \mathrm{i}\omega/\omega_{\mathrm{cut}} \approx 1$, meaning that the electrical circuit has no effect, so $U(t) = U_{\mathrm{app}}(t)$. The expression Eq. (39) is therefore exact at low frequencies, even for large values of W_s. Above the cutting frequency, the voltage is no longer uniform on the electrodes, while the model still assumes a uniform distribution. The correction of W_s by the RC circuit should therefore only be seen as a qualitative way to account for the decrease of the excitation amplitude above ω_{cut}.

Finally, using Eq. (39) in the constitutive relations Eqs. (31) and (32) yields:

$$\bar{s}_1 = \frac{J_m}{J_m - I_1 + 3}\left(\lambda_1 - {\lambda_1}^{-3}{\lambda_2}^{-2}\right) - \alpha_c \frac{\Gamma}{\bar{H}^2}\lambda_1\lambda_2^2 - \frac{\epsilon W}{\mu H_0^2}\frac{\Gamma}{\bar{H}^2}\lambda_1\lambda_2^2 , \tag{40}$$

$$\bar{s}_2 = \frac{J_m}{J_m - I_1 + 3}\left(\lambda_2 - {\lambda_1}^{-2}{\lambda_2}^{-3}\right) - \alpha_c \frac{\Gamma}{\bar{H}^2}\lambda_1^2\lambda_2 - \frac{\epsilon W}{\mu H_0^2}\frac{\Gamma}{\bar{H}^2}\lambda_1^2\lambda_2 , \tag{41}$$

where $\alpha_c = \epsilon U_c^2/\mu H_0^2$. In both equations, the first term is the mechanical stress, the second is the stress created by the static voltage, and the third is the dynamical stress due to the alternating component of the excitation voltage. This last term is proportional to W_s, meaning the excitation force depends linearly on the audio signal.

3.4. Summary of equations

To conclude this section, the complete set of equations comprises:

- the equilibrium equations (29), (30),
- the ideal gas law (34), used only when the cavity is closed,
- the boundary conditions (33),
- the constitutive relations (40) and (41).

The following section is devoted to the numerical solving of the system of equations described above, and to the calculation of the acoustic radiation.

4. Numerical solving

The resolution using finite elements is performed in two main stages: first the static equilibrium reached by the membrane when a given pressure and static voltage are applied is computed, and then the linear dynamics around this equilibrium are analyzed.

4.1. Solving for the static deformation

The equilibrium equations need to be transformed into a weak form in order to be implemented in the finite element software FreeFem++. We define the test functions v and w which satisfy $v(1) = 0$ and $w(0) = w(1) = 0$, and a test scalar $\mathcal{B}$. By multiplying the equilibrium equations (40), (41) and (34) by the test functions v, w, and $\mathcal{B}$, integrating by parts and using the boundary conditions (33), a residual is defined:

$$\begin{aligned}\mathfrak{R}([\bar{r},\bar{z},\beta],[v,w,\mathcal{B}]) = &\int_0^1 v'\frac{\bar{H}(\bar{R})\bar{R}\bar{s}_1\bar{z}'}{\lambda_1}\mathrm{d}\bar{R} - \int_0^1 \beta\bar{r}\bar{r}'v\mathrm{d}\bar{R} + \int_0^1 w'\frac{\bar{H}(\bar{R})\bar{R}\bar{s}_1\bar{r}'}{\lambda_1}\mathrm{d}\bar{R} + \int_0^1 \beta\bar{r}\bar{z}'w\mathrm{d}\bar{R} + \int_0^1 \bar{H}(\bar{R})\bar{s}_2 w\mathrm{d}\bar{R}\\ &+ (\beta_{\mathrm{atm}}+\beta)\mathcal{B}\left(\bar{V}_s + 2\pi\int_0^1 \bar{r}\bar{z}\bar{r}'\mathrm{d}\bar{R}\right)^{\gamma} - (\beta_{\mathrm{atm}}+\beta_{\mathrm{pres}})\mathcal{B}(\bar{V}_s+\bar{V}_{\mathrm{ini}})^{\gamma}\ . \end{aligned} \tag{42}$$

The static equilibrium equation then simply reads:

$$\mathfrak{R}([\bar{r},\bar{z},\beta],[v,w,\mathcal{B}]) = 0\ ,\forall[v,w,\mathcal{B}]\ . \tag{43}$$

This equation is solved using Newton-Raphson's method. First an initial guess of the solution is made in the form of a spherical cap. Then the residual $\mathfrak{R}([\bar{r},\bar{z},\beta],[v,w,\mathcal{B}])$ is linearized to provide the gradient for Newton-Raphson's method. Introducing the variables $\bar{r} = \bar{r}_0 + x_r$, $\bar{z} = \bar{z}_0 + x_z$ and $\beta = \beta_0 + x_\beta$, the linearized weak form reads:

$$\mathfrak{R}([\bar{r}_0,\bar{z}_0,\beta_0],[v,w,\mathcal{B}]) + \left\langle \mathfrak{R}'([\bar{r}_0,\bar{z}_0,\beta_0],[v,w,\mathcal{B}])\ ,\ [x_r,x_z,x_\beta]\right\rangle = 0\ . \tag{44}$$

The explicit linearized form of Eq. (44) is provided in Appendix A. The linear equation (44) is solved at each step of Newton-Raphson's method to find the increment $\bar{\mathbf{x}} = [x_r, x_z, x_\beta]$. The initial guess is then updated: $\bar{\mathbf{x}}_{\mathbf{0}} = [\bar{r}_0, \bar{z}_0, \mathcal{B}_0] = \bar{\mathbf{x}}_{\mathbf{0}} + \bar{\mathbf{x}}$. This is repeated until $\bar{\mathbf{x}}$ is sufficiently small ($\|\bar{\mathbf{x}}\|_2 < 1\mathrm{e}^{-8}$).

FreeFem++ software [29] is used to assemble the stiffness matrix and the force vector, and to solve the non-linear inflation problem. 200 P2 elements along the radius are used. The resolution is performed in two steps:

1. The static deformation created by the pre-stretch and the inflation pressure with no applied voltage is computed. In this step the pressure is prescribed: $\beta = \beta_{\mathrm{pres}}$ is an external parameter. The equation $PV^\gamma = \mathrm{cst}$ of Eq. (34) is removed from the weak form.
2. The static deformation created by the applied voltage is computed. The amount of gas in the volume is now fixed, and the inflation pressure may vary. The pressure β becomes a variable that has to be solved for. The same Newton-Raphson's method is used.

The complete static problem now depends on seven non-dimensional parameters: β_{pres}, α_c, J_m, ρ_{ratio}, β_{atm}, $\bar{a}$ and $\bar{V}_s$. At the end of this iterative solving, $\mathfrak{R}([\bar{r}_0,\bar{z}_0,\beta_0],[v,w,\mathcal{B}]) = 0$. Thus, $[\bar{r}_0,\bar{z}_0,\beta_0]$ is the static solution. Usually, approximately 20 Newton-Raphson iterations are needed for the first step, and 10 for the second.

4.2. Modal analysis

In order to compute the modes of the membrane around the static equilibrium, small harmonic perturbations around this equilibrium are introduced:

$$\bar{r} = \bar{r}_0 + x_r\mathrm{e}^{\mathrm{i}\bar{\omega}\bar{t}}\ ,\quad \bar{z} = \bar{z}_0 + x_z\mathrm{e}^{\mathrm{i}\bar{\omega}\bar{t}}\ ,\quad \beta = \beta_0 + x_\beta\mathrm{e}^{\mathrm{i}\bar{\omega}\bar{t}}\ ,\quad \lambda_1 = \lambda_{10} + x_{\lambda_1}\mathrm{e}^{\mathrm{i}\bar{\omega}\bar{t}}\ ,\quad \lambda_2 = \lambda_{20} + x_{\lambda_2}\mathrm{e}^{\mathrm{i}\bar{\omega}\bar{t}}\ . \tag{45}$$

The right hand side of the weak form Eq. (43) is modified to take into account inertia:

$$\mathfrak{R}([\bar{r},\bar{z},\beta],[v,w,\mathcal{B}]) = \bar{\omega}^2\int_0^1\left(1+\frac{\Gamma}{\bar{H}}\rho_{\mathrm{ratio}}\right)\bar{H}\bar{R}(vx_z + wx_r)\mathrm{d}\bar{R}\ ,\quad \forall[v,w,\mathcal{B}]\ . \tag{46}$$

The residual $\mathfrak{R}$ is linearized around the static solution $[\bar{r}_0, \bar{z}_0, \beta_0]$. As this is a static equilibrium $\mathfrak{R}([\bar{r}_0, \bar{z}_0, \bar{\beta}_0], [v, w, \mathcal{B}]) = 0$ for all test functions. Therefore the governing equation for linear vibrations is:

$$\left\langle \mathfrak{R}'([\bar{r}_0, \bar{z}_0, \beta_0], [v, w, \mathcal{B}]) \, , \, [x_r, x_z, x_\beta] \right\rangle - \bar{\omega}^2 \Phi([x_r, x_z], [v, w]) = \Psi([\bar{r}_0, \bar{z}_0, \beta_0], W_s) \, , \quad \forall [v, w, \mathcal{B}] \, , \tag{47}$$

where the first left-hand term is a bi-linear form in $[v, w, \mathcal{B}]$ and $[x_r, x_z, x_\beta]$ depending on the static solution that defines the stiffness matrix, Φ is a bi-linear form in $[x_r, x_z]$ and $[v, w]$ that defines the mass matrix, and $\Psi([\bar{r}_0, \bar{z}_0, \beta_0], W_s)$ is the force vector. Finally Eq. (47) can be written in the following matrix form, after discretization by finite elements:

$$\begin{bmatrix} \mathbf{K_{rz}} & \mathbf{K_{c12}} \\ \mathbf{K_{c21}} & K_\beta \end{bmatrix} \begin{bmatrix} \begin{bmatrix} x_r \\ x_z \end{bmatrix} \\ x_\beta \end{bmatrix} - \bar{\omega}^2 \begin{bmatrix} \mathbf{M_{rz}} & \mathbf{0} \\ \mathbf{0} & 0 \end{bmatrix} \begin{bmatrix} \begin{bmatrix} x_r \\ x_z \end{bmatrix} \\ x_\beta \end{bmatrix} = \begin{bmatrix} \mathbf{F_{rz}} \\ 0 \end{bmatrix} \tag{48}$$

$$\Leftrightarrow (-\bar{\omega}^2 \boldsymbol{\mathcal{M}} + \boldsymbol{\mathcal{K}}) \bar{\mathbf{x}} = \boldsymbol{\mathcal{F}} \tag{49}$$

where $\mathbf{K_{rz}}$ and $\mathbf{M_{rz}}$ are the membrane stiffness and mass matrices, $\mathbf{K_{c12}}$ and $\mathbf{K_{c21}}$ are the stiffness coupling terms between the membrane and the cavity stiffness, and K_β is the cavity stiffness. The weak form as expressed in Eq. (47) is not symmetric. Therefore the mass and stiffness matrices are not symmetric either. The standard modal orthogonality relations don't hold, but computing left- and right-modes allows to define bi-orthogonality relations [30]. Setting the right hand side to zero (no applied alternating voltage) defines the right eigenvalue problem. The left eigenvalue problem is obtained by transposing the system. The right mode shapes are denoted $\boldsymbol{\psi}_n^R$, the left mode shapes $\boldsymbol{\psi}_n^L$, and the eigenfrequencies $\bar{\omega}_n$. The equations defining the modes are:

$$\boldsymbol{\mathcal{K}} \boldsymbol{\psi}_n^R - \bar{\omega}_n^2 \boldsymbol{\mathcal{M}} \boldsymbol{\psi}_n^R = 0 \, , \tag{50}$$

$$\boldsymbol{\psi}_n^L \boldsymbol{\mathcal{K}} - \bar{\omega}_n^2 \boldsymbol{\psi}_n^L \boldsymbol{\mathcal{M}} = 0 \, . \tag{51}$$

Equations (50) and (51) are solved on FreeFem++ and 40 modes are computed. The eigenfrequencies and the mode shapes are found to be real.

4.3. Synthesis of calculated transfer functions

To compute the response of the membrane to the excitation by the electrodes, the dynamics are projected on the modal basis. The modal forces need to be evaluated, and then bi-orthogonality relations will provide the modal amplitudes. The kinematics can be expressed on the modal basis:

$$\bar{\mathbf{x}} = \sum_{n=1}^{N_{\text{modes}}} c_n \boldsymbol{\psi}_n^R \, . \tag{52}$$

Inserting Eq. (52) into Eq. (49), and pre-multiplying by the p-th left mode yields:

$$\sum_{n=1}^{N_{\text{modes}}} c_n \left(\boldsymbol{\psi}_p^L \boldsymbol{\mathcal{K}} \boldsymbol{\psi}_n^R - \omega^2 \boldsymbol{\psi}_p^L \boldsymbol{\mathcal{M}} \boldsymbol{\psi}_n^R \right) = \boldsymbol{\psi}_p^L \boldsymbol{\mathcal{F}} \, . \tag{53}$$

As all eigenvalues are of order one, bi-orthogonality relations between the right and left modeshapes hold, and the modal amplitudes of the forced response reads:

$$c_p = \frac{F_p}{\mu_p (\bar{\omega}_p^2 - \bar{\omega}^2)} \, , \tag{54}$$

where the modal force F_p is:

$$F_p = \boldsymbol{\psi}_p^L \boldsymbol{\mathcal{F}} = -\frac{\epsilon W_s}{\mu H_0^2} \frac{1}{1 + \mathrm{i} \frac{\bar{\omega}}{\bar{\omega}_{\text{cut}}}} \bar{F}_p \, , \tag{55}$$

with

$$\bar{F}_p = \int_{\bar{R}=0}^{1} \left(\bar{R} \frac{\Gamma}{\bar{H}} \lambda_{20}^2 \left((\psi_{p,z}^L)' \bar{z}_0' + (\psi_{p,r}^L)' \bar{r}_0' \right) + \frac{\Gamma}{\bar{H}} \lambda_{10}^2 \lambda_{20} \psi_{p,r}^L \right) \mathrm{d}\bar{R} \ , \tag{56}$$

where $\psi_{p,r}^L$ and $\psi_{p,z}^L$ denote the r and z components of the left mode shape p. The modal mass μ_p is:

$$\mu_p = \boldsymbol{\psi}_p^L \boldsymbol{\mathcal{M}} \boldsymbol{\psi}_p^R = - \int_{\bar{R}=0}^{1} \bar{R} \left(1 + \Gamma \rho_{\mathrm{ratio}}\right) \left(\psi_{p,r}^L \psi_{p,r}^R + \psi_{p,z}^L \psi_{p,z}^R \right) \mathrm{d}\bar{R} \ . \tag{57}$$

The transfer function between the excitation signal W_s and the membrane non-dimensional displacement $\bar{\mathbf{X}}$ can finally be expressed as:

$$H(\bar{\omega}, \bar{R}) = \frac{\bar{\mathbf{x}}}{W_s} = - \frac{\epsilon}{\mu H_0^2} \frac{1}{1 + \mathrm{i} \frac{\bar{\omega}}{\bar{\omega}_{\mathrm{cut}}}} \sum_{n=1}^{N_{\mathrm{modes}}} \frac{\bar{F}_n \boldsymbol{\psi}_n^R}{\mu_n (\bar{\omega}_n^2 - \bar{\omega}^2)} \ . \tag{58}$$

4.4. Damping model

The chosen material model is hyperelastic and loss-free. However, the losses will have a large influence on the dynamical behavior of the system, and have to be accounted for. The loss factor of most modes will be measured experimentally, but as some modes could not be measured, a loss factor estimation is required in the model. We chose to use a Rayleigh damping model [31], fitted on the experimental modal damping ratios (see section 5.4.1 for the experimental data).

In case of Rayleigh damping, the damping matrix is proportional to the mass and stiffness matrices: $\mathbf{C} = a_r \boldsymbol{\mathcal{M}} + b_r \boldsymbol{\mathcal{K}}$. This is very convenient since the undamped modes also diagonalize the damped system [31]. The only change is that the eigenfrequencies become complex numbers. As a consequence, the numerical modal analysis can be performed without any damping, and the eigenfrequencies are modified afterwards. The damping ratio for a Rayleigh-damped system reads [31]:

$$\xi_n = \frac{a_r}{2\omega_n} + \frac{b_r \omega_n}{2} \ . \tag{59}$$

This description of the damping is likely to be a huge simplification of the various real damping phenomena. For example, Fox et Goulbourne [8] found that their system had complex mode shapes, indicating that the damping phenomena are richer than the simple Rayleigh damping considered here. However they studied VHB membranes, which are likely to be much more heavily damped than the silicone membranes used in the present study. The transfer function Eq. (58) with the damping included finally reads:

$$H(\bar{\omega}, \bar{R}) = - \frac{\epsilon}{\mu H_0^2} \frac{1}{1 + \mathrm{i} \frac{\bar{\omega}}{\bar{\omega}_{\mathrm{cut}}}} \sum_{n=1}^{N_{\mathrm{modes}}} \frac{\bar{F}_n \boldsymbol{\psi}_n^R}{\mu_n (\bar{\omega}_n^2 + 2\mathrm{i}\xi_n \bar{\omega} \bar{\omega}_n - \bar{\omega}^2)} \ . \tag{60}$$

4.5. Radiated acoustic pressure

This section presents the computation of the sound radiation of the membrane, whose velocity is considered to be known. The definition of the dimensional variables used in this section is given in Fig. 4. The radiated acoustic pressure can be computed using a Rayleigh integral. This formula describes exactly the radiation of a flat vibrating surface in an infinite baffle. In practice it works for a baffle large compared to the acoustic wavelength ($\lambda \gg b$). The radiated pressure is expressed as:

$$P(\mathbf{r_p}, \omega) = -\rho_O \omega^2 \int_S x(\mathbf{r}, \omega) \frac{\mathrm{e}^{-\mathrm{i}k|\mathbf{r_p} - \mathbf{r_0}|}}{2\pi |\mathbf{r_p} - \mathbf{r_0}|} \mathrm{d}S \ . \tag{61}$$

This expression has been modified by Quægebeur et al. to take into account the effect of the curvature of the source [32]. This is valid for small curvatures ($t_{\max} \ll a$). They formulated the Rayleigh integral in the time domain, but it can easily be adapted to the frequency domain:

$$P(\mathbf{r_p}, \omega) = -\rho_O \omega^2 \int_S G(\mathbf{r_p}, \mathbf{r_0}, \omega) \, \mathbf{X}(\mathbf{r_0}, \omega) \cdot \mathbf{n} \, \mathrm{d}S \ , \tag{62}$$

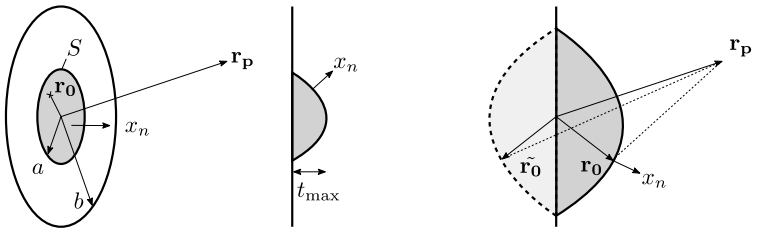

Figure 4: Definition of the variables used for the Rayleigh integral, and modified Rayleigh integral for sound radiation by inflated membranes using image sources.

with

$$G(\mathbf{r_p}, \mathbf{r_0}, \omega) = \frac{\mathrm{e}^{-\mathrm{i}k|\mathbf{r_p}-\mathbf{r_0}|}}{4\pi|\mathbf{r_p}-\mathbf{r_0}|} + \frac{\mathrm{e}^{-\mathrm{i}k|\mathbf{r_p}-\tilde{\mathbf{r}}_0|}}{4\pi|\mathbf{r_p}-\tilde{\mathbf{r}}_0|} \,, \tag{63}$$

where $\tilde{\mathbf{r}}_0$ is the symmetric of the source with respect to the baffle.

Quægebeur et al. compared their computations for rigid shells to exact results calculated by Suzuki and Tichy [33], and found good agreement over almost the whole frequency range. For a spherical cap with $t_{\max} \approx 0.75a$, there was a difference up to 5 dB around $ka = 1$ due to diffraction effects that are not taken into account in this model. At lower and higher frequencies ($ka < 0.5$ and $ka > 3$), the modified Rayleigh integral predicts the radiated pressure within 1 dB.

The transfer function between the excitation voltage W_s and the radiated pressure can finally be computed as:

$$H_p(\bar{\omega}) = \frac{P}{W_s} = \frac{\rho_0 \epsilon}{\rho H_0^2} \frac{1}{\left(1 + \mathrm{i}\,\frac{\bar{\omega}}{\bar{\omega}_{\mathrm{cut}}}\right)} \sum_{n=1}^{N_{\mathrm{modes}}} \frac{\bar{\omega}^2 \bar{F}_n R_n(\bar{\omega})}{\mu_n(\bar{\omega}_n^2 + 2\mathrm{i}\xi_n\bar{\omega}\bar{\omega}_n - \bar{\omega}^2)} \,, \tag{64}$$

where R_n is a modal radiation term:

$$R_n(\bar{\omega}) = \int_0^1 \left(-\psi_{n,r}^R \bar{z}_0' + \psi_{n,z}^R \bar{r}_0'\right) \bar{r}_0 \left(\frac{\mathrm{e}^{-\mathrm{i}\bar{k}\bar{A}|\bar{\mathbf{r}}_\mathbf{p}-\bar{\mathbf{r}}_\mathbf{0}|}}{2|\bar{\mathbf{r}}_\mathbf{p}-\bar{\mathbf{r}}_\mathbf{0}|} + \frac{\mathrm{e}^{-\mathrm{i}\bar{k}\bar{A}|\bar{\mathbf{r}}_\mathbf{p}-\bar{\tilde{\mathbf{r}}}_\mathbf{0}|}}{2|\bar{\mathbf{r}}_\mathbf{p}-\bar{\tilde{\mathbf{r}}}_\mathbf{0}|}\right) \mathrm{d}\bar{R} \,, \tag{65}$$

with $\bar{k} = Ak$, $\bar{\mathbf{r}}_\mathbf{0} = \mathbf{r_0}/A$, $\bar{\mathbf{r}}_\mathbf{p} = \mathbf{r_p}/A$, and $\bar{\tilde{\mathbf{r}}}_\mathbf{0} = \tilde{\mathbf{r}}_\mathbf{0}/A$.

5. Experimental validation of the coupled electromechanical model

In this section the numerical model is validated by different experiments: static, dynamic and acoustic measurements.

5.1. Experimental setup

The experimental setup for the validation of the numerical results for the static deformation is shown in Fig. 5. The membrane is put on a circular frame, without any pre-stretch. The back volume is pressurized to a pressure P, which is measured by a Furness control manometer. A DC voltage is applied to the electrodes using a TREK 609E-6 high voltage amplifier. The new pressure in the back cavity is recorded. The laser displacement sensor is moved over the membrane using a Newport linear stage, to measure the deflection in z direction on one diameter. The membrane is inflated at four different pressures (P = 500, 1000, 1500 and 2000 Pa). For each case, four different voltages are applied (U_c = 0, 1000, 2000 and 3000 V).

The experimental setup and signal processing flow chart for dynamical measurements are shown in Fig. 6. The applied voltage is now built of a DC and an alternating component, in a manner to suppress the first harmonic of the non-linear force (see section 3.3). The alternating signal $W_s(t)$ is a white noise filtered to the frequency band of interest [50–1000 Hz]. The z component of the membrane velocity is measured using a laser scanning vibrometer (Polytec PSV-500), on a mesh of 450 points evenly distributed over the membrane. The transfer function between the white

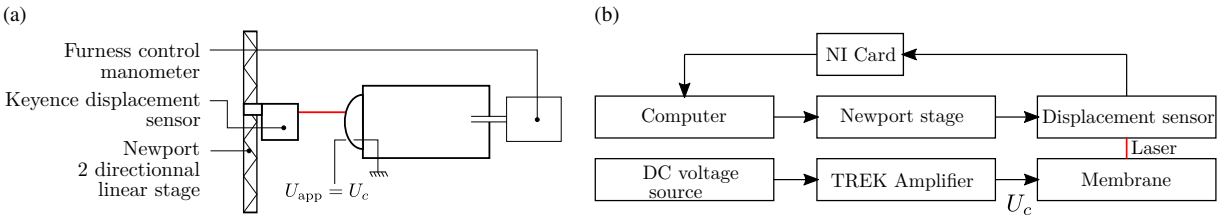

Figure 5: Setup for static measurements. (a) Schematic of the setup. (b) Block diagram.

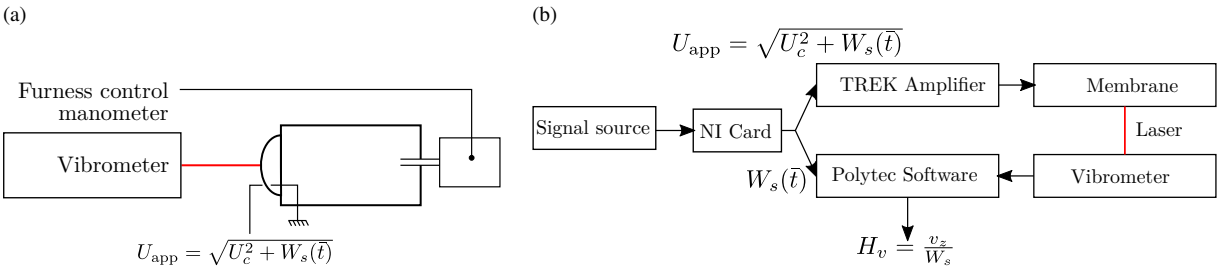

Figure 6: Setup for dynamic measurements. (a) Schematic of the setup. (b) Block diagram.

noise W_s and the velocity is computed by averaging over 6 measurements for each point. The frequency resolution is 0.78 Hz. This step results in a transfer function $H_v = v_z/W_s$ for each point of the mesh, where v_z is the membrane velocity along z. The transfer functions can be fed into a modal analysis program to extract the eigenfrequencies, the mode shapes, and the modal damping ratios. To obtain the following results, the *Least-Square Complex Exponential* method (LSCE) has been used [34].

To perform the acoustical measurements, the prototype is placed in a circular baffle of radius $b = 0.7$ m, and put into an anechoic chamber specified down to 120 Hz. A microphone is located on axis at a distance of 1 m. The experimental transfer function between the acoustic pressure P and W_s is obtained using the Welch method for spectral averaging.

5.2. Parameters identification

5.2.1. Membrane thickness

The silicone membrane is spin-coated, and its thickness is measured using a laser displacement sensor (Keyence LK-G37), and also using a microscope. The thickness profile is plotted in Fig. 7. It appears that due to the spin-coating process the membrane thickness is not uniform. To allow the use of the measured thickness in the finite

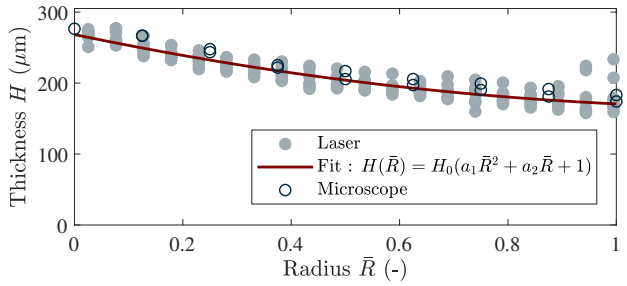

Figure 7: Measured thickness of the membrane as a function of the non-dimensional radius. The fitting parameters are $H_0 = 268\,\mu$m, $a_1 = 0.23$, and $a_2 = -0.59$.

element simulation, the thickness should be defined as an analytical function of the radius. A simple 3-parameter function $H(\bar{R}) = H_0(a_1\bar{R}^2 + a_2\bar{R} + 1)$ is thus fitted on the measurements, and also plotted in Fig. 7.

5.2.2. Constitutive parameters

The parameters of the Gent constitutive material law μ and J_m have been measured by a bi-axial inflation test following the method proposed by Rosset et al. [35]. We used the NuSil CF19-2186 silicone, and the parameters we found are close (within 7%) to those found by other researchers [35, 36] (see Table 1). The differences may be due to the fabrication process, like for example the amount of solvent used to decrease the viscosity before spin-coating the membrane, or the curing temperature. The value of the electrical permittivity of the silicone is taken from [37].

5.2.3. Electrode resistivity and membrane capacitance

The electrodes are made of carbon grease, and are painted on the membrane by hand. The impedance of the prototype is measured using the voltage and current monitor outputs of the TREK amplifier, and plotted in Fig. 8 together with the fitted theoretical impedance of the model sketched in Fig. 3.

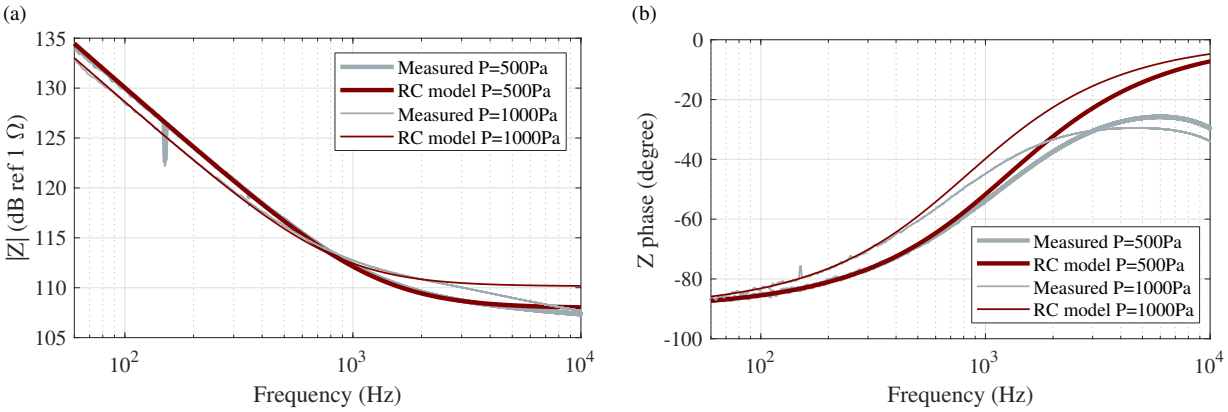

Figure 8: Electrical behavior of the dielectric elastomer membrane. (a) Impedance amplitude. (b) Impedance phase. The RC model is plotted with $R = 2.5 \times 10^5\ \Omega$, $C = 502$ pF for $P = 500$ Pa, and $R = 3.2 \times 10^5\ \Omega$, $C = 590$ pF for $P = 1000$ Pa.

Figure 8 shows that the electrical model correctly captures the electrical behavior of the membrane. However at high frequencies, above 2000 Hz, the phase is no longer correctly predicted. The impedance becomes indeed very small and comparable to that of the TREK amplifier, so the measured impedance starts being dominated by the amplifier impedance. The electrical cutting frequency is found to be $f_{\text{cut}} = 1/2\pi R_e C = 1381$ Hz, for the parameters given in Tab. 1.

5.2.4. List of all parameters

The parameters used for all experiments presented in this article are listed in Table 1. All these parameters have been measured by independent experiments, or found in the literature. The shear modulus μ is the only parameter that is adjusted, so that the computed static deformation fits the measured one (see Fig. 9(a)). After this adjustment, the shear modulus differs from the one measured by the bi-axial inflation test by 13%. This uncertainty comes from the difficulty to measure precisely μ with the bi-axial inflation test, especially when the membrane thickness if not uniform.

5.3. Results

5.4. Static deformation

The membrane deformation for four different prescribed pressures and no applied voltage is plotted in Fig. 9(a). The displacement of the membrane caused by the applied voltage is plotted in Fig. 9(b) for one value of the prescribed

Dim.	Value	Non-dim.	Value	Dim.	Value	Non-dim.	Value	Dim.	Value	Non-dim.	Value
H_0	268 µm	-	-	V_s	1.04 L	$\bar{V}_s$	16.4	R_{elec}	2.85 cm	R_{elec}/A	0.71
μ	2.3×10^5 Pa	-	-	P	500 Pa	β	0.324	ρ	1042 kg m^{-3}	-	-
J_m	44	J_m	44	U_c	2000 V	α	0.0060	ρ_{elec}	0.11 kg m^{-2}	ρ_{ratio}	0.39
A	4 cm	-	-	W_s	500 V^2	-	-	ϵ_r	2.8	-	-
a	4 cm	$\bar{a}$	1	P_{atm}	1.013 hPa	β_{atm}	65.7	f_{cut}	1266 Hz	-	-
-	-	a_1	0.23	-	-	a_2	-0.59				

Table 1: List of all experimental dimensional parameters (Dim.) and non-dimensional parameters (Non-dim.). These parameters are used in all experiments and numerical results presented in the present paper, except when it is specified that it is not the case.

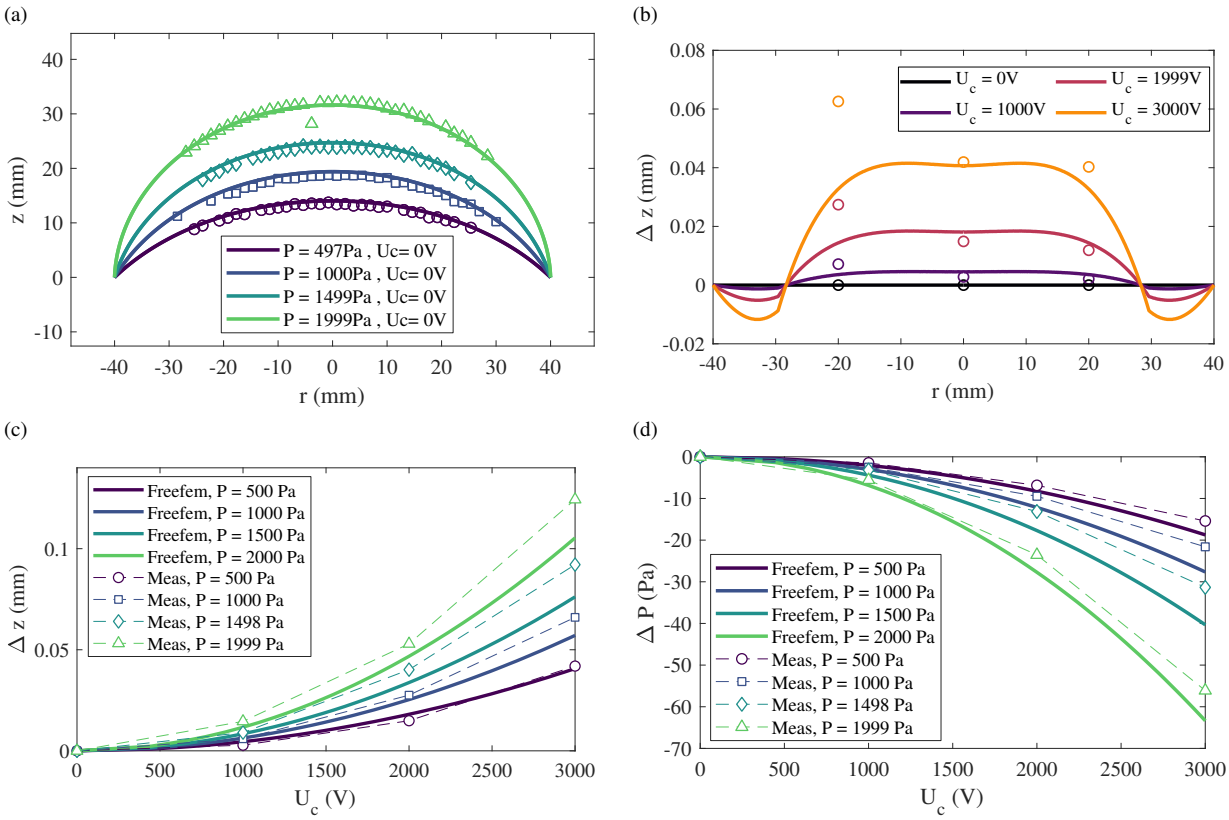

Figure 9: Solid lines: numerical results, markers: measurements. The pressure in the legend is the inflation pressure when no voltage is applied ($U_c = 0$). (a) Membrane deformation when no voltage is applied. (b) Displacement along z of the membrane when a voltage is applied, the pressure is fixed at 500 Pa. (c) Deflection of the center point when a voltage is applied. The displacement is relative to the position of the center point when no voltage is applied ($U_c = 0$). (d) Variation of the static pressure when a voltage is applied.

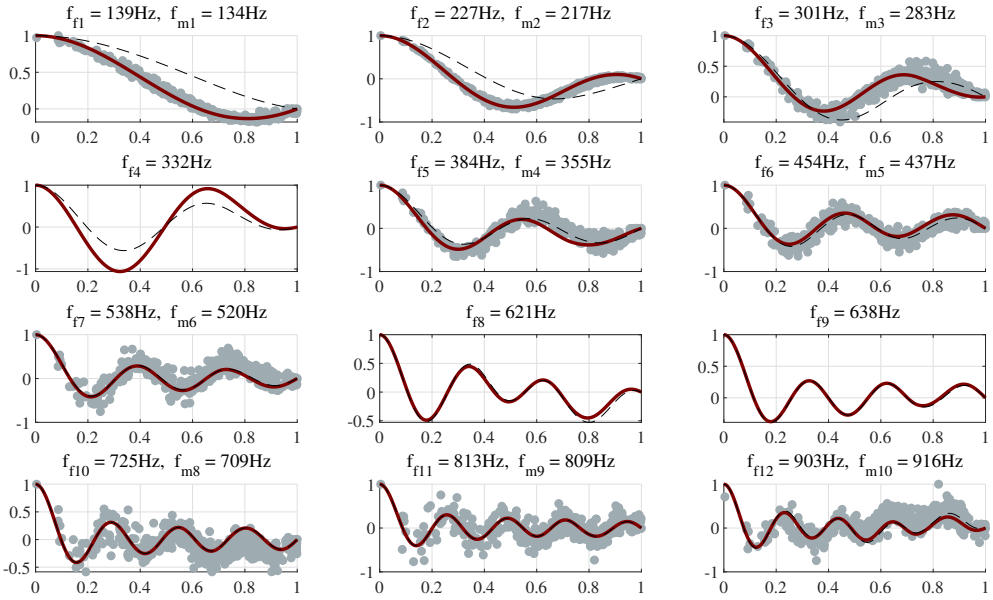

Figure 10: Comparison of the measured and computed eigenmodes. The dots are the measured modes, and the line the computed ones. The dashed lines are the computed modes with $\bar{V}_s = \infty$. f_{fi} is the frequency of the i^{th} computed mode, and f_{mi} the frequency of the i^{th} measured mode. The x-axis is the non-dimensional radius, and the y-axis is the scaled mode shape amplitude. The mode shapes were measured on a mesh covering the full membrane. All points of the mesh are plotted here, which allows to check whether the modes are really axisymmetric.

pressure. The displacement of the apex of the membrane for the four inflation pressures is plotted in Fig. 9(c). The measured and computed equilibrium pressures after the voltage is applied are given in Fig. 9(d).

Figure 9 shows that the model accurately describes the finite deformation of the membrane when both a static pressure and a voltage are applied. The coupling with the cavity stiffness (that enforces an adiabatic evolution inside the cavity) is able to predict the pressure drop created by the voltage. The present model where a Gent material law is used allows to compute the deformation for large pressures. The model using a Neo-Hookean behavior studied by Zhu et al. in [14] is limited to small pressures ($\beta \lesssim 0.5$). Indeed without the stiffening at large strains modeled by the parameter J_m in Gent's law, the membrane exhibits snap-through instability. This instability has not been observed experimentally here, and is not observed numerically either when Gent's law is used.

Figure 9(b) shows that the membrane displacement is not perfectly axisymmetric, and this might explain some of the differences observed in other experiments. The negative displacement in Fig. 9(b) at radius $r > 30$ mm occurs in the area of the membrane which not covered by the electrode. As the voltage is applied only where electrodes are present, the stress distribution changes compared to the unactivated case. This may result in different displacements in the different areas.

5.4.1. Modal analysis

The mode shapes of the membrane with the parameters given in Table 1 are measured using the method presented in section 5.1, and computed using the numerical method presented in section 4.2. The computed modes, which are real are scaled so that the maximum amplitude is 1. The measured modes are complex, so a little more attention has to be paid to their scaling, which is done as follows. The point with maximum amplitude is used as a phase reference: the phase of the whole mode is adjusted so that the phase of this point is zero. The real part of this phase-adjusted mode is scaled to a maximum amplitude of 1, and plotted. The computed modes 4, 8 and 9 have not been measured, so they are not plotted in Fig. 10. Most likely the modal force of these modes was too small to create a significant modal displacement.

Figure 10 shows an overall good agreement between the measured and the computed mode shapes. Contrary to Fox and Goulourne [10], our measured modes are almost real. Silicone was used in the present experiments, whereas Fox and Goulbourne used VHB which is known to have a higher loss factor [38].

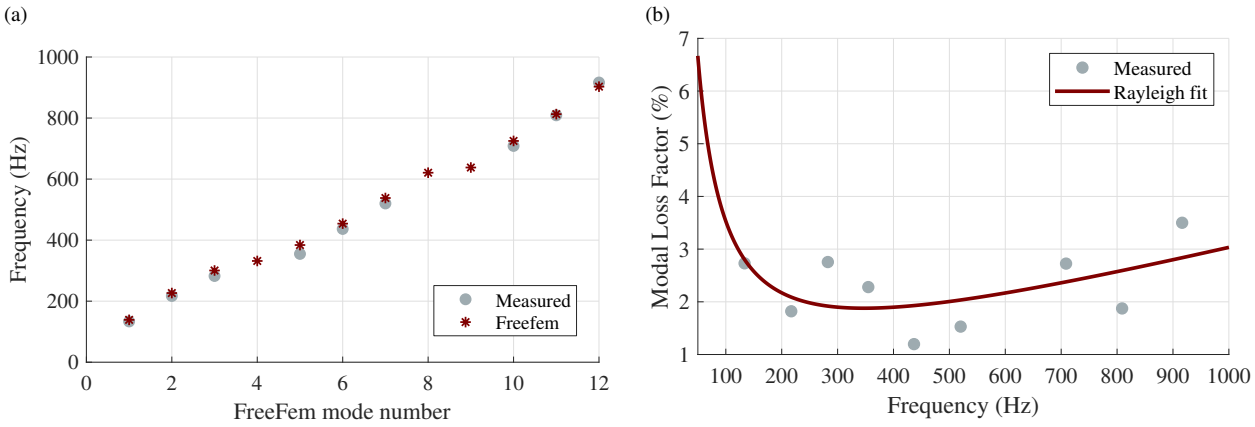

Figure 11: a) Measured and computed eigenfrequencies. b) Measured modal loss factors and Rayleigh fit. The damping matrix reads $\mathbf{C} = a_r \boldsymbol{\mathcal{M}} + b_r \boldsymbol{\mathcal{K}}$ with $a_r = 6.51$ s and $b_r = 5.4 \times 10^{-5}$ s^{-1}.

The mode shapes computed with an infinite value of $\bar{V}_s$ are also shown, which corresponds to neglecting the stiffness added by the cavity. The results highlight that taking this effect into account is of primary importance, in particular at low frequencies where the volume displaced by the modes is large.

The eigenfrequencies fit well, as seen in Fig. 11(a), and a fitted Rayleigh damping seems to be a fair approximation of the measured damping ratios (Fig. 11(b)).

5.5. *Frequency response functions*

The experimental and numerical results are now compared in terms of frequency response functions. These results are presented here in order to assess the validity of the model and clarify its limits, before analysing and discussing the influence of different parameters on the radiated pressure in section 6.

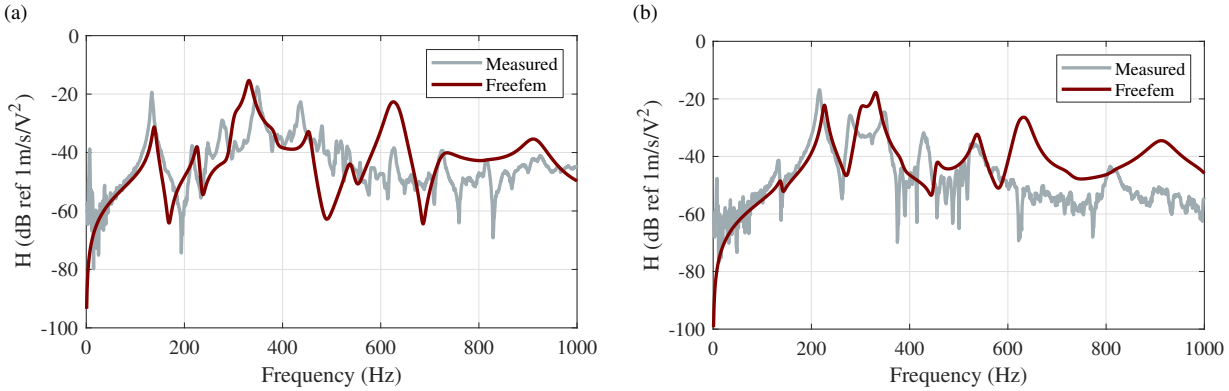

Figure 12: Computed and measured transfer function between the z component of the velocity and the excitation voltage W_s. (a) Average on 3 points around radius $\bar{R} = 0.3$. (b) Average on 14 points around radius $\bar{R} = 0.6$.

First, the transfer functions between the excitation signal W_s and the velocity in the z direction of the membrane are plotted at two different radius in Fig. 12. At low frequencies, below 400 Hz, the dynamics of the membrane are well captured by the model. The amplitude of the resonances is reasonably well predicted, even if it is overestimated for some modes, like the peak at 600 Hz. This is most likely due to imperfections of the prototype. One possible problem is that the electrode thickness is not uniform. If the electrode is too thin at some locations, the resistivity will become very large, and the charges will not have the time to dispatch evenly on the membrane. The uniform voltage assumption that is made in the model is no longer valid in that case.

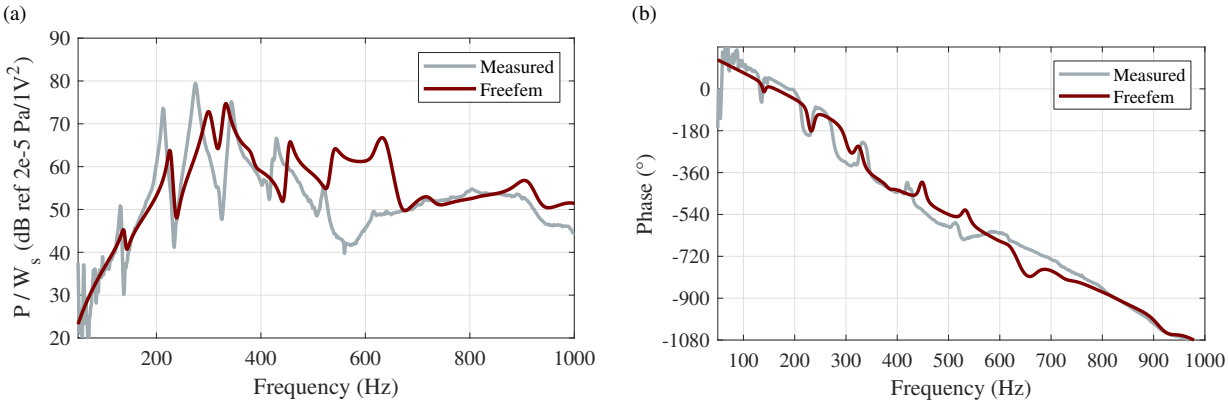

Figure 13: Computed and measured transfer functions between the radiated pressure and the excitation signal W_s. (a) Amplitude. (b) Phase in degrees.

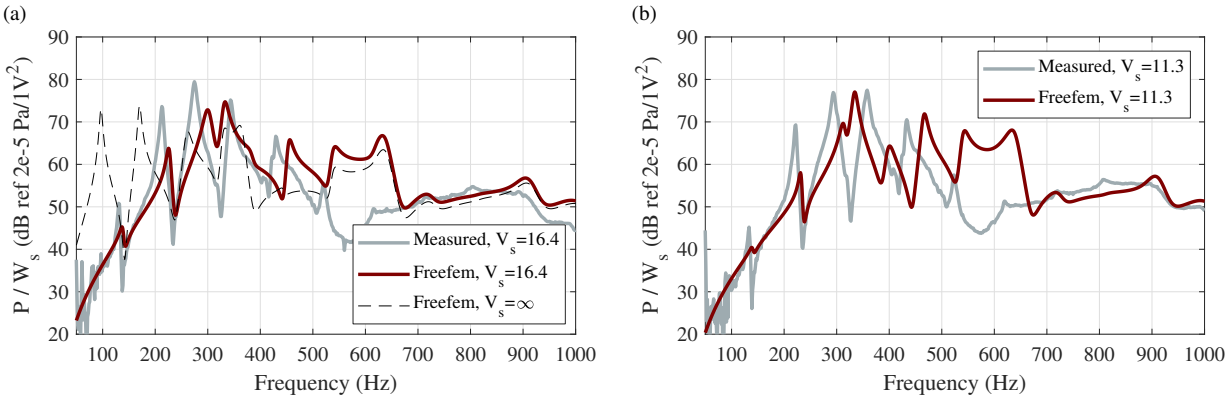

Figure 14: Computed and measured transfer functions between the radiated pressure and the excitation signal W_s. (a) Back cavity volume $\bar{V}_s = 16.4$. (b) Back cavity volume $\bar{V}_s = 11.3$.

The next comparison is performed on the acoustic pressure radiated by the loudspeakers. For the set of parameters given in Table 1, the numerical and experimental transfer functions between the acoustic pressure on axis at 1 m and the excitation signal W_s are plotted in Fig. 13. Figure 13(a) shows that the model accurately predicts the radiated acoustic pressure at low frequencies, below 500 Hz. There are though small errors on modal frequencies, and some errors on the peak levels (up to 7 dB for the mode around 200 Hz). At higher frequencies there are larger differences, for the reasons explained above. The phase shown in Fig. 13(b) is also correctly predicted.

6. Discussion

The objective of this section is to analyse and discuss the influence of some parameters on the behavior of the loudspeaker. Most analyses and comparisons will be performed on the acoustical transfer functions, because acoustics is what matters the most for a use as a loudspeaker, and also because the calculation giving the radiated pressure involves all modeling steps.

6.1. Influence of the back cavity volume

The back cavity volume induces an added stiffness that is exerted on each dynamical mode of the membrane. Neglecting the stiffness resulting from the cavity is equivalent to assuming an infinite volume V_s. For the set of parameters given in Table 1, the numerical transfer function between the radiated pressure and W_s are plotted for

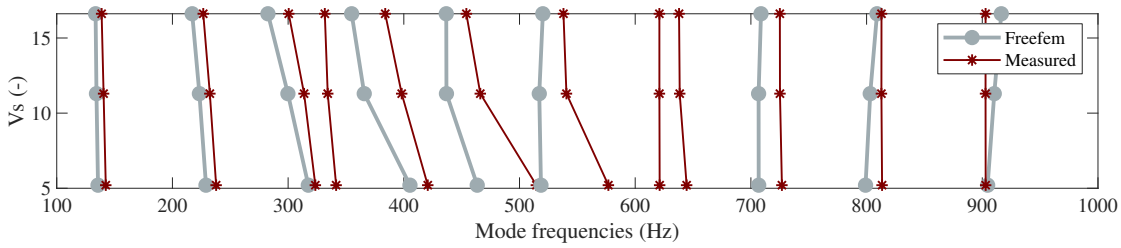

Figure 15: Influence of the back cavity volume on the eigenfrequencies of the dielectric membrane. Each vertical line represents one mode.

Pressure (Pa)	500	1000	1500	2000
f_{cut} (Hz)	1266	832	518	217

Table 2: Electrical cutting frequency of the membrane for different inflation pressures.

$\bar{V}_s = 16.4$ in Fig. 14(a) and for $\bar{V}_s = 11.3$ in Fig. 14(b). Additionally in Fig. 14(a), the acoustic pressure that would be obtained if the cavity stiffness were neglected is also plotted. The lower frequency part of the transfer function is strongly changed and does not fit anymore with the experimental data, highlighting the importance of taking this stiffness into account.

When the volume of the cavity is reduced (Fig. 14(b)), two effects can be observed: the level of the low frequency peaks is reduced, and the eigenfrequencies of most of the modes increase. This result is due to the added stiffness, which is more important for the first modes, as seen in Fig. 10. These effects are also predicted by the model. The eigenfrequencies are plotted as function of the cavity volume in Fig. 15, where the increase of most frequencies when the cavity volume is reduced is clearly visible. For most of the modes the increase in frequency is correctly predicted by the model, but not for the modes around 500 Hz. These modes are those that radiate the most efficiently, as seen in Fig. 14. It is thus expected that the coupling between these modes and the acoustical radiation is stronger compared with other modes. Extending the model to take into account the strong coupling between the membrane dynamics and acoustics might therefore be of large interest.

6.2. Influence of the inflation pressure

Keeping this time the back cavity volume constant, the inflation pressure is now varied. The radiated pressure is plotted for four different values of the inflation pressure in Fig. 16. This figure shows that the model better predicts the acoustic radiation for small inflation pressures. It should be noted that the same discrepancy is observed on velocity transfer function even though it is not presented here. An important parameter for the analysis of the plots in Fig. 16 is the electrical cutting frequency (see section 3.3), which is given in Table 2 for the four inflation pressures.

The electrical cutting frequency decreases sharply for large inflation pressures. This effect results from the combination of a capacity increase due to the area increase and of the thinning of the membrane, and of a resistivity increase due to the thinning of the electrodes. As discussed earlier, once the forcing reaches f_{cut}, the voltage is not uniform over the membrane. This effect is not accounted for in the model. Consequently, the modal forces of the modes above f_{cut} will not be correctly predicted, thus explaining the differences seen in Fig. 16. The present model (section 3.3) hence just accounts for the global trend which is a decrease of the modal forces above f_{cut}. Considering the electrodynamical loading of the dielectric elastomer membrane appears to be important to capture the high frequency behavior, and deserves further studies.

What is more, the larger the inflation pressure the thinner the membrane. As a consequence the fluid loading becomes relatively more important for large pressures and the fact that it has not been taken into account might also explain the observed discrepancies for larger inflation pressures. Deriving a fully coupled fluid/structure model could improve these results.

7. Conclusion

The field of dielectric loudspeakers remains little explored. In order to advance in understanding the key mechanisms of this type of transducers, we have presented a complete study of a typical system, from the modeling of

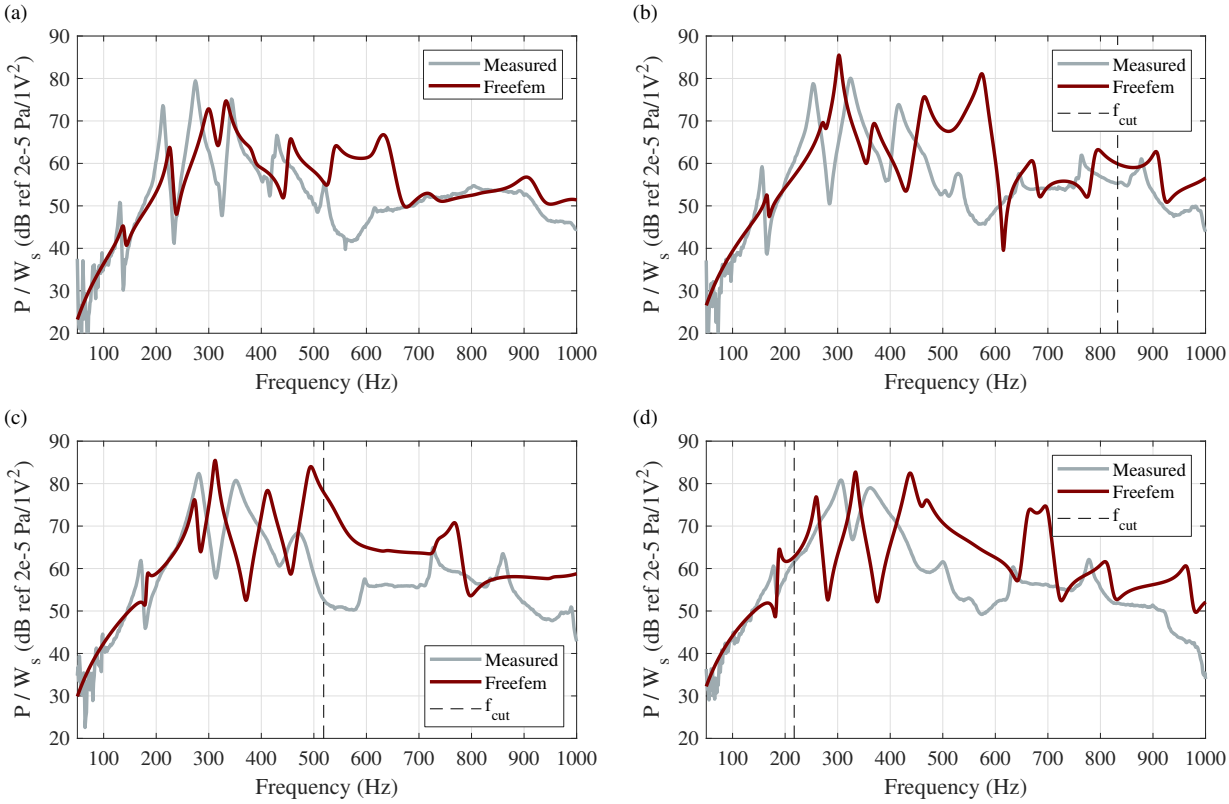

Figure 16: Computed and measured transfer functions between the radiated pressure and the excitation signal W_s. Each figure corresponds to a given inflation pressure. (a) 500 Pa. (b) 1000 Pa. (c) 1500 Pa. (d) 2000 Pa.

the electromechanical continuous medium, to the calculation of acoustic frequency response functions. A systematic comparison with experiments validated the modeling and highlighted its potential limitations. In particular, key features like the back cavity effect have been included and shown to be of primary importance on the radiated pressure.

The two key phenomena that should be taken into account to extend the range of application are the strong coupling with acoustics, because of the very lightweight membrane we consider; and the electrodynamical loading (due to the resistivity of the electrodes, the voltage is no longer uniform over the membrane at high frequencies). Predicting the dynamic voltage distribution would allow for the computation of accurate modal forces even at high frequencies.

It is hoped that this model will help to perform an efficient optimization of dielectric elastomer loudspeakers. This approach allowing to explore numerically all sets of key parameters is novel, and should help improving significantly the performance of this type of loudspeakers.

Acknowledgments

The authors acknowledge the support of the French National Research Agency (ANR) within the project SMArT (ANR-15-CE08-0007-02).

Appendix A. Linearized weak form for finite element solving

The expression of the linearized residual is given here. It is used both in the Newton-Raphson algorithm to compute the non-linear static deformation, and for the calculation of the eigenmodes and eigenvalues. The bars over non-dimensional variables are omitted in this appendix.

$$
\begin{aligned}
\mathfrak{R}([r_0+x_r, z_0+x_r, \beta+x_\beta], [v, w, \mathcal{B}]) = \\
&- \int \beta_0 r_0 r_0' v \mathrm{d}R + \int \beta_0 r_0 z_0' w \mathrm{d}R + \int v' \frac{R s_{10}}{\lambda_{10}} z_0' \mathrm{d}R + \int w' \frac{R s_{10}}{\lambda_{10}} r_0' \mathrm{d}R + \int s_{20} w \mathrm{d}R \\
&+ (\beta_{\mathrm{atm}} + \beta_0)\tilde{\beta}\left(V_s + 2\pi \int r_0 z_0 r_0' dR\right)^\gamma - (\beta_{\mathrm{atm}} + \beta_{\mathrm{ini}})\tilde{\beta}(V_s + V_{\mathrm{ini}})^\gamma \\
&+ \int v' \frac{R\tilde{s}_1}{\lambda_{10}} z_0' \mathrm{d}R - \int v' \frac{R s_{10}}{\lambda_{10}^2} z_0' \tilde{\lambda}_1 \mathrm{d}R + \int v' \frac{R s_{10}}{\lambda_{10}} x_z' \mathrm{d}R + \int w' \frac{R\tilde{s}_1}{\lambda_{10}} r_0' \mathrm{d}R - \int w' \frac{R s_{10}}{\lambda_{10}^2} r_0' \tilde{\lambda}_1 \mathrm{d}R + \int w' \frac{R s_{10}}{\lambda_{10}} x_r' \mathrm{d}R \\
&- \int \beta_0 (x_r r_0' + r_0 x_r') v \mathrm{d}R + \int \beta_0 (x_r z_0' + r_0 x_z') w \mathrm{d}R + \int \tilde{s}_2 w \mathrm{d}R - \int x_\beta r_0 r_0' v \mathrm{d}R + \int x_\beta r_0 z_0' w \mathrm{d}R \\
&+ (\beta_{\mathrm{atm}} + \beta_0) 2\pi\gamma \int (r_0 z_0 x_r' + r_0 x_z r_0' + x_r z_0 r_0') \mathrm{d}R \mathcal{B}\left(V_s + 2\pi \int r_0 z_0 r_0' \mathrm{d}R\right)^{\gamma-1} + x_\beta \mathcal{B}\left(V_s + 2\pi \int r_0 z_0 r_0' \mathrm{d}R\right)^\gamma \qquad \text{(A.1)}
\end{aligned}
$$

where s_{10}, s_{20}, λ_{10}, λ_{20} are evaluated for r_0, z_0 and β_0, and variables with a tilde $\tilde{}$ are the linearized terms (e.g. $s_1 = s_{10} + \tilde{s}_1 + O([x_r^2, x_z^2, x_\beta^2])$, $\tilde{s}_1$ being linear in $[x_r, x_z, x_\beta]$).

References

[1] R. Pelrine, R. Kornbluh, Q. Pei, J. Joseph, High-Speed Electrically Actuated Elastomers with Strain Greater Than 100%, Science 287 (5454) (2000) 836–839. doi:10.1126/science.287.5454.836.

[2] F. Xia, S. Tadigadapa, Q. Zhang, Electroactive polymer based microfluidic pump, Sensors and Actuators A: Physical 125 (2) (2006) 346–352. doi:10.1016/j.sna.2005.06.026.

[3] I. A. Anderson, T. Hale, T. Gisby, T. Inamura, T. McKay, B. O'Brien, S. Walbran, E. P. Calius, A thin membrane artificial muscle rotary motor, Applied Physics A 98 (1) (2010) 75–83. doi:10.1007/s00339-009-5434-5.

[4] H. F. Schlaak, M. Jungmann, M. Matysek, P. Lotz, Novel multilayer electrostatic solid state actuators with elastic dielectric (Invited Paper), in: Y. Bar-Cohen (Ed.), Smart Structures and Materials, San Diego, CA, 2005, p. 121. doi:10.1117/12.604468.

[5] G. P. Rosati Papini, G. Moretti, R. Vertechy, M. Fontana, Control of an oscillating water column wave energy converter based on dielectric elastomer generator, Nonlinear Dynamics 92 (2) (2018) 181–202. doi:10.1007/s11071-018-4048-x.

[6] R. Heydt, R. Kornbluh, R. Pelrine, V. Mason, Design and performance of an electrostrictive polymer-film acoustic actuator, Journal of Sound and Vibration 215 (2) (1998) 297–311. doi:10.1006/jsvi.1998.1642.

[7] R. Heydt, R. Pelrine, J. Joseph, J. Eckerle, R. Kornbluh, Acoustical performance of an electrostrictive polymer film loudspeaker, The Journal of the Acoustical Society of America 107 (2) (2000) 833–839.

[8] J. W. Fox, N. C. Goulbourne, On the dynamic electromechanical loading of dielectric elastomer membranes, Journal of the Mechanics and Physics of Solids 56 (8) (2008) 2669–2686. doi:10.1016/j.jmps.2008.03.007.
[9] R. Heydt, R. Kornbluh, J. Eckerle, R. Pelrine, Sound radiation properties of dielectric elastomer electroactive polymer loudspeakers, in: Smart Structures and Materials 2006: Electroactive Polymer Actuators and Devices (EAPAD), Vol. 6168, International Society for Optics and Photonics, San Diego, California, USA, 2006, p. 61681M. doi:10.1117/12.659700.
[10] J. W. Fox, N. C. Goulbourne, Electric field-induced surface transformations and experimental dynamic characteristics of dielectric elastomer membranes, Journal of the Mechanics and Physics of Solids 57 (8) (2009) 1417–1435. doi:10.1016/j.jmps.2009.03.008.
[11] N. Hosoya, S. Baba, S. Maeda, Hemispherical breathing mode speaker using a dielectric elastomer actuator, The Journal of the Acoustical Society of America 138 (4) (2015) EL424–EL428. doi:10.1121/1.4934550.
[12] E. M. Mockensturm, N. Goulbourne, Dynamic response of dielectric elastomers, International Journal of Non-Linear Mechanics 41 (3) (2006) 388–395. doi:10.1016/j.ijnonlinmec.2005.08.007.
[13] J. Zhu, S. Cai, Z. Suo, Nonlinear oscillation of a dielectric elastomer balloon, Polymer International 59 (3) (2010) 378–383. doi:10.1002/pi.2767.
[14] J. Zhu, S. Cai, Z. Suo, Resonant behavior of a membrane of a dielectric elastomer, International Journal of Solids and Structures 47 (24) (2010) 3254–3262. doi:10.1016/j.ijsolstr.2010.08.008.
[15] Y. Li, I. Oh, J. Chen, Y. Hu, A new design of dielectric elastomer membrane resonator with tunable resonant frequencies and mode shapes, Smart Materials and Structures (Mar. 2018). doi:10.1088/1361-665X/aab996.
[16] W. Hong, Modeling viscoelastic dielectrics, Journal of the Mechanics and Physics of Solids 59 (3) (2011) 637–650. doi:10.1016/j.jmps.2010.12.003.
[17] H. Wang, M. Lei, S. Cai, Viscoelastic deformation of a dielectric elastomer membrane subject to electromechanical loads, Journal of Applied Physics 113 (21) (2013) 213508. doi:10.1063/1.4807911.
[18] Z. Wang, T. He, Electro-viscoelastic behaviors of circular dielectric elastomer membrane actuator containing concentric rigid inclusion, Applied Mathematics and Mechanics 39 (4) (2018) 547–560. doi:10.1007/s10483-018-2318-8.
[19] Y. Li, I. Oh, J. Chen, H. Zhang, Y. Hu, Nonlinear dynamic analysis and active control of visco-hyperelastic dielectric elastomer membrane, International Journal of Solids and Structures (May 2018). doi:10.1016/j.ijsolstr.2018.05.006.
[20] W. Kaal, S. Herold, Electroactive Polymer Actuators in Dynamic Applications, IEEE/ASME Transactions on Mechatronics 16 (1) (2011) 24–32. doi:10.1109/TMECH.2010.2089529.
[21] B. D. Coleman, W. Noll, The thermodynamics of elastic materials with heat conduction and viscosity, Archive for rational mechanics and analysis 13 (1) (1963) 167–178.
[22] A. Kovetz, Electromagnetic Theory, Oxford University Press, Oxford, New York, 2000.
[23] J. Edmiston, D. Steigmann, Analysis of Nonlinear Electrostatic Membranes, in: Mechanics and Electrodynamics of Magneto- and Electro-Elastic Materials, CISM International Centre for Mechanical Sciences, Springer, Vienna, 2011, pp. 153–180. doi:10.1007/978-3-7091-0701-0_4.
[24] L. Dorfmann, R. W. Ogden, Nonlinear Theory of Electroelastic and Magnetoelastic Interactions, Springer US, Boston, MA, 2014.
[25] Z. Suo, Theory of dielectric elastomers, Acta Mechanica Solida Sinica 23 (6) (2010) 549–578. doi:10.1016/S0894-9166(11)60004-9.
[26] A. N. Gent, A New Constitutive Relation for Rubber, Rubber Chemistry and Technology 69 (1) (1996) 59–61. doi:10.5254/1.3538357.
[27] J. E. Adkins, R. S. Rivlin, Large elastic deformations of isotropic materials IX. The deformation of thin shells, Phil. Trans. R. Soc. Lond. A 244 (888) (1952) 505–531. doi:10.1098/rsta.1952.0013.
[28] A. Libai, J. G. Simmonds, The Nonlinear Theory of Elastic Shells, Cambridge university press, Cambridge, UK, 2005.
[29] F. Hecht, New development in freefem++, Journal of Numerical Mathematics 20 (3-4) (2013) 251–266. doi:10.1515/jnum-2012-0013.
[30] F. Ma, T. K. Caughey, Analysis of Linear Nonconservative Vibrations, Journal of Applied Mechanics 62 (3) (1995) 685–691. doi:10.1115/1.2896001.
[31] R. W. Clough, J. Penzien, Dynamics of Structures., McGraw-Hill, New York, 1993.
[32] N. Quaegebeur, A. Chaigne, G. Lemarquand, Transient modal radiation of axisymmetric sources: Application to loudspeakers, Applied Acoustics 71 (4) (2010) 335–350. doi:10.1016/j.apacoust.2009.10.003.
[33] H. Suzuki, J. Tichy, Sound radiation from convex and concave domes in an infinite baffle, The Journal of the Acoustical Society of America 69 (1) (1981) 41–49. doi:10.1121/1.385248.
[34] D. L. Brown, R. J. Allemang, R. Zimmerman, M. Mergeay, Parameter Estimation Techniques for Modal Analysis, SAE Transactions 88 (1979) 828–846.
[35] S. Rosset, L. Maffli, S. Houis, H. R. Shea, An instrument to obtain the correct biaxial hyperelastic parameters of silicones for accurate DEA modelling, in: Proc. SPIE 9056, San Diego, California, USA, 2014, p. 90560M. doi:10.1117/12.2044777.
[36] N. C. Goulbourne, E. M. Mockensturm, M. I. Frecker, Electro-elastomers: Large deformation analysis of silicone membranes, International Journal of Solids and Structures 44 (9) (2007) 2609–2626. doi:10.1016/j.ijsolstr.2006.08.015.
[37] F. Carpi, D. De Rossi, R. Kornbluh, R. E. Pelrine, P. Sommer-Larsen, Dielectric Elastomers as Electromechanical Transducers, Elsevier, Amsterdam, 2011.
[38] S. Michel, X. Q. Zhang, M. Wissler, C. Löwe, G. Kovacs, A comparison between silicone and acrylic elastomers as dielectric materials in electroactive polymer actuators, Polymer International 59 (3) (2010) 391–399. doi:10.1002/pi.2751.